EUROPEAN ORGANIZATION FOR NUCLEAR RESEARCH

CERN-EP/84-163
29 November 1984

PRECISE MEASUREMENTS OF PROTON-ANTIPROTON AND PROTON-PROTON TOTAL CROSS-SECTIONS AT THE CERN INTERSECTING STORAGE RINGS

G. Carboni[1], D. Lloyd Owen[2] and K. Potter

CERN, Geneva, Switzerland

M. Ambrosio, G. Barbarino, G. Paternoster and S. Patricelli

Dipartimento di Fisica dell'Università and INFN, Naples, Italy

V. Cavasinni, T. Del Prete, M. Morganti, F. Schiavo and M. Valdata-Nappi[3]

Dipartimento di Fisica dell'Università and INFN, Pisa, Italy

G. Anzivino[4] and P.D. Grannis

State University of New York, Stony Brook, NY, USA

(Submitted to Nuclear Physics B)

---

1) On leave of absence from INFN, Pisa, Italy.
2) Present address: State University of New York, Stony Brook, NY, USA.
3) On leave of absence. Present address: Indiana University, Bloomington, Ind., USA.
4) Present address: CERN, Geneva, Switzerland

ABSTRACT

A detailed account is given of high-precision measurements of the total hadronic cross-sections of proton-antiproton and proton-proton interactions at centre-of-mass energies of 30.6, 52.8, and 62.7 GeV. The experiment was performed at the CERN Intersecting Storage Rings (ISR) using the total-interaction-rate method, in which additive correction terms for trigger losses were held to less than 6% of the final result. An experimental determination of the vertical beam-displacement scale permitted luminosity-monitor calibrations to be made with high intrinsic accuracy. The over-all precision (systematic and statistical errors combined) achieved in the total cross-section was $\pm$1.1% for proton-antiproton reactions and the 0.7% for proton-proton reactions. In the proton-proton case the measurement was the most precise such measurement made at the ISR.

1. INTRODUCTION

The total cross-section (σ_{tot}) is one of the most important quantities characterizing the dynamics of a reaction, and depends only on the species of the initial-state particles and their centre-of-mass (c.m.) energy ($\sqrt{s}$). It is one of the first parameters to be measured when a particular reaction can be studied in a new energy regime, and an extensive body of data embracing a variety of initial states has been accumulated over the years.

Despite this impressive experimental achievement, the difficulties involved in deriving a total hadronic cross-section from first principles have not been overcome. Considerable theoretical effort has been focused on the general properties of scattering amplitudes in the framework of axiomatic field theory, exploiting unitarity, analyticity, and crossing symmetry, and has resulted in a number of theorems that limit the behaviour of cross-sections [1]. (The Pomeranchuk theorem on particle-antiparticle cross-section ratios [2] and the Froissart bound on total cross-sections [3] are two well-known examples.) While experimental measurements indicate no violation of field-theoretic assumptions, it must be noted that the constraints provided by such theorems are relatively weak , and the data have served rather to chart our progress towards asymptotia. Indeed, the inauguration of successive accelerators has led to a steady postponement of the onset of the asymptotic energy regime [4].

In the absence of a quantitative theory, phenomenological models have been developed to promote an understanding of hadronic interactions. In the late 1960's , when the available data indicated that most hadronic total cross-sections were falling with energy, models then prevailing [5] offered a broad spectrum of high-energy predictions. The generally favoured prediction was that cross-sections would decrease smoothly to a finite limit [6], but some models [7] foresaw vanishing cross-sections at infinite energy,

whilst still others [8] predicted the logarithmic increase permitted by the Froissart bound. New accelerators, then under construction, were eagerly awaited as the source of revelation.

Early indications that the decrease in total cross-sections [9] was not to continue indefinitely came from experiments [10] performed at the IHEP 70 GeV/c proton synchrotron. These experiments found a levelling off of all total cross-sections measured. In retrospect one sees that the top IHEP energy is just about the energy at which total cross-sections reach a minimum value, except in the case of $p\bar{p}$ and K^+p.

The discovery of a rise of $\sigma_{tot}(pp)$ came with the advent of the Intersecting Storage Rings (ISR). At equivalent momenta of up to 2000 GeV/c, the CERN-Rome [11] and Pisa-Stony Brook [12] Collaborations showed irrefutably that $\sigma_{tot}(pp)$ was rising having attained a minimum at $\sqrt{s} \simeq 10$ GeV [1] and, furthermore, that this rise would continue well beyond ISR energies [14]. (The definitive reports of ISR total cross-section experiments are listed under ref. [15]. They have been averaged by Amaldi and Schubert [16].)

Subsequent measurements at the FNAL 400 GeV/c proton synchrotron [17] found this rise to be the general behaviour of all measured hadronic total cross-sections. Only $\sigma_{tot}(p\bar{p})$ failed to give conclusive evidence of its now expected rise, until the introduction of antiprotons into the ISR in 1980 permitted the study of $p\bar{p}$ collisions in a new energy regime.

The over-all impression given by the results of several ISR experiments was the similarity of $p\bar{p}$ and pp interactions [18]. Where significant differences were observed [19], they were found to be small and probable manifestations of the different (anti)quark content of the proton and antiproton.

---

1) A rise in $\sigma_{tot}(pp)$ with a $\ln^2 s$ energy dependence had, in fact, been suggested a year earlier on the basis of cosmic-ray data [13].

As far as total cross-sections were concerned, evidence of the increase in $\sigma_{tot}(p\bar{p})$ was soon forthcoming from the Louvain-Northwestern Collaboration [20] and from this collaboration [21]. In addition, the cross-section difference $\sigma_{tot}(p\bar{p}) - \sigma_{tot}(pp)$ was seen to be diminishing with energy.

This article is a full account of our total cross-section measurements, and is organized as follows: in Section 2, we give a short description of the CERN antiproton project and of conditions of $p\bar{p}$ experimentation at the ISR. Section 3 outlines the experimental method. The measurement of luminosity was an integral part of the method, and the accuracy of this measurement depended critically on our knowledge of the ISR beam-displacement scale; the experimental calibration of this scale is described in Section 4. The apparatus and the data acquisition are described in Sections 5 and 6, respectively. Section 7 is a detailed exposition of experimental procedure and data analysis. Lastly, we present and discuss the final results in Section 8.

2. ANTIPROTONS AT THE ISR

The idea of storing antiprotons in the ISR was first discussed by Johnsen in 1962 [22], prior even to the construction of the ISR, and was re-examined [23] intermittently in following years.

It was recognized that the luminosity would be impractically low unless a means could be found to condense the phase-space volume occupied by antiproton pulses produced by target bombardment, to dimensions suitable for injection into the ISR. The invention of beam-cooling techniques [24] was thus of pivotal importance, and imparted renewed vigour to the proposal.

The final impetus came with the decision to convert the CERN Super Proton Synchrotron (SPS) into a $p\bar{p}$ collider, which entailed the local construction of an adequate antiproton source.

2.1 The antiproton source

The heart of the CERN antiproton complex is the Antiproton Accumulator (AA) [25], a ring of wide-aperture magnets located between the Proton Synchrotron (PS) and the ISR (fig. 1).

Antiprotons are generated by 26 GeV/c protons accelerated in the PS (10^{13} protons per pulse with a 2.4 s repetition rate) [26] interacting in the AA target. A linear magnetic horn at 0° collects $\bar{p}$'s produced in the forward direction with an angular acceptance of 50 msr and a momentum acceptance of $\Delta p/p = 1.5\%$ centred at 3.575 GeV/c. The collected $\bar{p}$'s, typically 10^6 per pulse, are injected into the AA ring.

The injected pulse is pre-cooled stochastically from $\Delta p/p = 1.5\%$ to $\Delta p/p = 0.2\%$ in an outer orbit by a system of pick-ups and kickers. Movable shutters separate the injected pulse from the accumulated stack during this stage to avoid perturbative cross-talk. The shutters are then opened, and the pulse is decelerated by an RF cavity to move it into the stack ($p_{stack} = 3.5$ GeV/c). The whole operation from injection to stacking occurs between consecutive PS pulses.

The stack is cooled continuously both transversally and in momentum by another pick-up/kicker system, so that $\bar{p}$'s in the stack migrate to create a dense core at the inner orbit. After about 24 hours of AA operation, the stack contains $\simeq 10^{11}$ $\bar{p}$'s, roughly 60% of which form the core.

When the core is sufficiently dense, a part of it is accelerated to the extraction orbit and transferred to the PS (via TTL2 and TT2 in fig. 1). The $\bar{p}$'s circulate counter-clockwise (the 'wrong' direction) during acceleration in the PS, and are then sent to the ISR (via TT6 and TT1) for injection into Ring 2.

2.2 Running conditions

Total cross-section data were collected in dedicated ISR running periods during which the machine was operated in a special mode to reduce the transverse dimensions of the beam-overlap zone. Such a reduction in source size was necessary in order to optimize the geometrical definition of detector components, particularly for the elastic scattering measurement of this and the Louvain-Northwestern experiments, both of which were installed in intersection No. 2 (I2).

This mode, the Terwilliger (TW) scheme [27], was achieved with a special set of quadrupole magnets deployed around both rings. When correctly energized, the TW quadrupoles imparted kicks to off-momentum particles in such a way that all particles, independently of momentum, intersected the closed orbit in the even-numbered intersections. The beam width, and thus the source size, in these intersections was then determined solely by horizontal betatron oscillations.

The effect of the Terwilliger scheme at other azimuths was to double the beam widths, reducing the available horizontal aperture and limiting the beam currents that could be stored to $\lesssim$ 10 A. This, then, was the proton current for $p\bar{p}$ running.

The p and $\bar{p}$ beams stored in the ISR were subjected to stochastic cooling both vertically and in momentum, which led to exceptionally stable beam conditions. Nevertheless, over a period of hours the p beam developed a halo, which resulted in increased background due to interactions with ambient material upstream from I2. When this background had evolved to a certain level, the halo was removed using movable scrapers [28] installed in I3.

The extremely stable $\bar{p}$ beam was retained for periods of about 10 days. During this time, the p beam was replaced with more or less its usual

periodicity without disturbing the $\bar{p}$ beam. A profile in time of one of the $p\bar{p}$ runs is shown in fig. 2. It is a testimony to the remarkable skill of the ISR operations team.

The first $p\bar{p}$ run at the ISR took place in April, 1981, when about 6×10^9 $\bar{p}$'s were successfully stored, yielding a current $I_2 = (306 \pm 10)$ μA and a luminosity $L \simeq 10^{26}$ cm^{-2} s^{-1}. Even at such low luminosities, a 5% measurement (Carboni et al. [21]) of $\sigma_{tot}(p\bar{p})$ was achieved. A major contribution to the error in σ_{tot} at that time arose from the $\bar{p}$ current measurement devices (current transformers [29]). This uncertainty was substantially reduced (to ±1 μA) for subsequent runs.

The $p\bar{p}$ results presented here come from three later ISR running periods, details of which are given in table 1.

The pp results come chiefly from shorter runs immediately prior to or subsequent to the $p\bar{p}$ running periods; runs unassociated with the $p\bar{p}$ runs also contributed. The beam currents were typically 3 A, and the TW scheme was employed.

3. OUTLINE OF THE METHOD

The $p\bar{p}$ and pp total cross-sections were measured using the total-rate method:

$$\sigma_{tot} = R_{tot}/L \ , \qquad (1)$$

where R_{tot} is the total hadronic interaction rate of the colliding beams and L is their luminosity, both quantities being measured simultaneously. The method was pioneered by the Pisa-Stony Brook Collaboration [30], and has the advantages of simplicity and directness.

The ability to detect every interaction implies a fully efficient coverage of the complete solid angle around the zone where the interactions occur. This was not entirely possible at the ISR because of the holes that had to remain uncovered to accommodate the vacuum chambers of the incoming and exiting beams. The most important loss associated with these holes was that of elastic interactions (strongly peaked in the forward direction) in which the scattered particles did not emerge from the vacuum chambers of the exiting beams. Inelastic interactions of a diffractive type were also lost when the quasi-elastically scattered particle remained in the vacuum chamber. These losses were estimated as additive correction terms to the observed cross-section:

$$\sigma_{tot} = \sigma_{obs} + \Delta\sigma_{el} + \Delta\sigma_{in}$$

with

$$\sigma_{obs} = R_{obs}/L \ . \qquad (2)$$

The correction terms were calculated by extrapolating a measured angular distribution to the forward direction, and then integrating it over the region of dead space. The magnitude of the combined correction was kept small by minimizing the solid angle subtended by the holes, and ranged from 2.5% to 6% of σ_{tot}, increasing with beam momentum.

The initial-state charge of the $p\bar{p}$ reaction is zero, thus for the $p\bar{p}$ measurement there was a potential insensitivity in the apparatus that was not present in the pp case. Topological $p\bar{p}$ cross-sections have been measured at energies below ISR energies, and we present the extrapolated zero-prong cross-section in fig. 3. As the figure shows, the loss associated with this effect is insignificant.

The expression for the luminosity is straightforward at the ISR, where the beams cross at a finite angle in the horizontal plane ($\alpha_{ISR} = 14.77°$) and each beam is uniformly populated around its circuit. The luminosity depends on the overlap of the beams in the vertical dimension (z) only:

$$L = \frac{1}{K_{ISR}} \int \frac{dI_1(z)}{dz} \frac{dI_2(z + \delta)}{dz} dz \ , \tag{3}$$

where δ is the separation of the beam centroids, and the current densities are normalized to the total currents I_1 and I_2. The factor K_{ISR} depends on the velocities β_1 and β_2 of the beams:

$$K_{ISR} = \frac{e^2 c \sin \alpha_{ISR}}{\sqrt{\frac{1}{\beta_1^2} + \frac{1}{\beta_2^2} + \frac{2 \cos \alpha_{ISR}}{\beta_1 \beta_2} - \sin^2 \alpha_{ISR}}} \ . \tag{4}$$

In the case of symmetric beams ($\beta_1 = \beta_2 = \beta$) this reduces to

$$K_{ISR} = \frac{\beta e^2 c \sin (\alpha_{ISR}/2)}{\sqrt{1 - \beta^2 \sin^2 (\alpha_{ISR}/2)}} = \beta \ 0.9972 \ 10^{-28} \ \text{cm s A}^2 \ . \tag{5}$$

The luminosity is measured following the method of van der Meer [31] (VdM). A telescope of counters is chosen as a monitor:

$$R_{mon} = \sigma_{mon} \ L \ , \tag{6}$$

where R_{mon} is the rate of the interactions that trigger the monitor and σ_{mon} is the inclusive cross-section for it. If the latter is known, the instantaneous luminosity can be derived directly from the monitor rate. To calibrate a monitor the ISR beams are steered vertically through each other, changing δ in small precise steps while recording $R_{mon}(\delta)$. The calibration constant σ_{mon} is then found by evaluating the integral:

$$\int R_{mon}(\delta)\, d\delta = I_1 I_2 \sigma_{mon}/K_{ISR} \,. \qquad (7)$$

4. THE CALIBRATION OF THE ISR BEAM-DISPLACEMENT SCALE

Measurements of cross-sections at the ISR are limited in their ultimate precision and accuracy by the albeit small uncertainty arising from the luminosity measurement, which sets the cross-section scale. The VdM method, acknowledged to be the best method of determining luminosity, requires the vertical displacement of the ISR beams [eq. (7)], and it is the uncertainty in this displacement scale that is the limiting factor.

Normally, beam-optics calculations provide the scale and, by comparing total cross-section measurements performed using the total-rate and optical-theorem methods, Amaldi et al. [15] showed that such calculations are reliable to $\pm 1\%$.

The present measurements, however, benefited from a direct calibration of this scale in the intersection where the total-cross-section measurements were made, using the most precise method known for finding the vertical centre of a beam circulating in the ISR.

Special beam scrapers were used to find the vertical positions of the beams. These scrapers were of the type described by Potter and Turner [32], and were installed on both beam lines 3.2 m upstream from the intersection point (fig. 4). Each scraper consisted of two tantalum blades, one above and one below the beam, mounted on separate, motor-driven carriages. In

order to find the vertical centre of the beam, the blades were stepped through the beam while recording the loss of beam current.

The edge of the tantalum blades were straight to within 10 μm along their 20 cm length, and were set horizontal to within 0.5 mrad. The screw mechanism driving the scrapers had an accuracy of 10 μm over a 10 cm range, and mechanical measurements were made to ensure that the blades were always within ±5 μm of their indicated position throughout that range. The overall precision in determining the centroid of a beam from scraper position and current data was ±3 μm.

To perform the calibration, a proton pulse was injected into the ISR, and displaced vertically using the same steering program as that used for luminosity calibrations. The pulse was then scraped away to find its centre, and the process repeated for a number of different nominal beam displacements. The results of a typical calibration are shown in fig. 5, where the difference in the measured position and the nominal position ($z_m - z_s$) is plotted as a function of the nominal position (z_s). The slope of the fitted straight line gives the deviation of the nominal scale from the true one [$z_m = z_s(1 + \varepsilon)$], and the residual indicates that the deviation was both linear and reproducible.

Calibrations were made, over a period of months, of both beam scales at three momentum settings (15, 22, and 26 GeV/c). The results showed that the nominal scale had to be corrected by a factor $(1 + \varepsilon) = (1.018 \pm 0.004)$, and that, within the errors, this factor was the same for the two beams and was independent of beam momentum.

Bryant and Potter [33] have reported these measurements in greater detail than above, and have investigated other systematic effects on the beam-displacement scale. Their conclusion is that all other systematic errors in the scale contribute an uncertainty of less than ±0.2%.

5. THE EXPERIMENTAL APPARATUS

The apparatus was installed in I2 because of two particularities of the ISR design. Firstly, the TW scheme (see subsection 2.2) was operative only in even-numbered intersections. Secondly, the distance from the crossing point to the nearest downstream magnet is greater in the even-numbered intersections (9.8 m in I2), where the beams coast from larger to smaller radii and require less bending around the ISR circumference in order to reach the next intersection. The greater distance permitted our detector to extend to smaller angles, minimizing dead-space losses.

The layout of the apparatus in I2 is shown in fig. 6. A solid-angle coverage for charged particles > 99.9% was achieved with ten scintillator-counter hodoscopes, five in each arm (CIO, H_{12}, H_{34}, H_5, TB). The left and right arms were mirror images of each other.

Each hodoscope consisted of two planes of trigger counters. The central hodoscopes CIO were in the form of open-ended boxes; the inner detector CI consisted of eight counters, and the outer detectors CO_L and CO_R each consisted of thirty counters. The H_{12} and H_{34} hodoscopes were roughly circular, centred on the exiting beams. The planes H_1 and H_2 of H_{12} consisted of twenty rectangular counters; the planes H_3 and H_4 of H_{34} consisted of eight large triangular counters. Hodoscopes H_5 and TB were rectangular, and the two counters in each plane were tailored to fit snugly around the exiting vacuum chamber. All hodoscopes covered the full azimuth, and neighbouring hodoscopes in each arm overlapped each other in polar angle.

The two planes of trigger counters in each hodoscope were operated in selective coincidence to minimize accidental firing: each counter in the plane closest to the source was placed in coincidence ($\Delta t = \pm 5$ ns) with

those in the second plane that the source projected it onto, the over-all hodoscope signal then being the logical sum (OR) of these individual coincidences.

The only dead spaces in the full detector were:

i) the holes in the TB hodoscopes for the exiting beams (0.086 msr in each arm);

ii) the holes in the H_{12} hodoscopes for the incoming beams (9 msr in each arm); and

iii) the cracks between abutting counters within hodoscope planes.

The holes in the TBs resulted in a significant loss of event-detection efficiency owing to the highly forward nature and low single-arm multiplicity of elastic and diffractive interactions. The solid angle subtended by the holes was minimized by locating the TBs as far downstream as possible (9.26 m from the crossing point), where the vacuum chamber narrowed to a roughly elliptical cross-section (with semi-axes of 7.85 and 3.00 cm).

The holes in the H_{12}s, although larger than those in the TBs, entailed an entirely negligible loss in sensitivity.

Finally, cracks between adjacent TB counters, which could have caused a significant loss in efficiency for single-diffractive interactions, were eliminated by overlapping rather than abutting the individual counters in these hodoscopes[2]. The small cracks in the larger-angle hodoscopes did not cause a measurable loss in trigger efficiency.

---

2) The Pisa-Stony Brook Collaboration, with a similar apparatus, found that the cracks in their TBs caused a loss corresponding to 1% σ_{tot} (Amaldi et al. [15]). Their experience led us to 'update' our detector at the outset by the inclusion of an extra hodoscope (H_5) as well as by overlapping TB counters.

Each trigger counter was equipped with a light-emitting diode (LED) which could be pulsed to simulate a minimum-ionizing particle. The on-line computer could fire any configuration of these LEDs, so that it was possible to test individual counters and to reproduce any trigger pattern (subsection 7.3).

The three H hodoscopes in each arm were equipped with a third plane of counters ($H_2\theta$, $H_4\theta$, $H_5\theta$) used to locate charged secondaries in polar angle and, to a lesser degree, in azimuth. These planes consisted of concentric rings of scintillator centred on the exiting beams, segmented into either quadrants or octants in azimuth. The polar coverage of the θ planes was $0.6^\circ < \theta < 31^\circ$ in each arm. In the total cross-section measurements, these hodoscopes were used to establish the angular distribution on which the inelastic-loss correction [$\Delta\sigma_{in}$, eq.(2)] was based.

The functioning of the more than 400 channels of scintillation counters was regularly checked both manually and via the data-acquisition system.

The apparatus included an elastic scattering detector and a vertex detector in addition to the scintillator hodoscopes. The elastic-scattering detector (described in Ambrosio et al. [21]) consisted of drift-tube hodoscopes, and contributed to this measurement by providing the slope parameters used in the calculation of the elastic losses [$\Delta\sigma_{el}$, eq.(2)]. The vertex detector was a system of modular drift chambers [34] sandwiched between the CI and CO hodoscopes, and was used here to study certain effects in the background subtraction (discussed in subsection 7.1).

6. DATA ACQUISITION

The main data-acquisition trigger, dubbed the fully inclusive (FI) trigger, required at least one track in any hodoscope in one arm in coincidence with at least one track in any hodoscope in the opposite arm:

$$T^{FI} = (ARM)_L^{FI} * (ARM)_R^{FI} \quad , \tag{8}$$

$$(ARM)_i^{FI} = (CIO + H_{12} + H_{34} + H_5 + TB)_i \; ; \quad i = L, R \; ,$$

where L (R) refers to the side of the incoming proton (antiproton) beam.

The timing of the main L * R coincidence was kept loose ($\Delta t = \pm 50$ ns) to ensure collection of all good triggers and to admit some background for monitoring purposes. The trigger corresponded, by definition, to the observed cross-section, and was the only trigger used in pp running.

Owing to the low luminosity and severe background in $p\bar{p}$ running, a second, small-angle (SA) trigger was used for $p\bar{p}$ luminosity-monitor calibrations:

$$T^{SA} = (ARM)_L^{SA} * (ARM)_R^{SA} \quad , \tag{9}$$

$$(ARM)_i^{SA} = (H_{34} + H_5 + TB)_i \; ; \quad i = L, R \; .$$

This was necessary in order to reduce the time taken for the calibration by minimizing the dead-time of the data acquisition.

The FI trigger was sensitive to 99% of all inelastic interactions, but also sensitive to single-beam interactions striking the central hodoscopes (H_{12} and CIO). The SA trigger, on the other hand, whilst still sensitive to between 74% (at $\sqrt{s}$ = 30.6 GeV) and 91% (at $\sqrt{s}$ = 62.7 GeV) of all inelastic events, was relatively insensitive to single-beam background. As an illustration, during $p\bar{p}$ running at $\sqrt{s}$ = 52.8 GeV, the signal-to-noise ratio of the FI trigger was 1/25, whereas it was 1/1 for the SA trigger.

When a trigger occurred, all relevant information was transferred by CAMAC to the on-line PDP-11/60 computer and written onto magnetic tape for subsequent analysis. This information comprised:

i) the hit pattern in all counters;

ii) the times of hodoscope signals with respect to the trigger; and

iii) the live-time of the data acquisition prior to the trigger.

The dead-time associated with this transfer amounted to about 3 ms per event.

7. EXPERIMENTAL PROCEDURE AND ANALYSIS OF DATA

7.1 Subtraction of background

A major concern of the data analysis was the identification and subtraction of background, of which single-beam (SB) interactions were by far the major source. Whereas true beam-beam (BB) interactions produced secondaries that radiated from the beam-overlap zone, SB interactions resulted in secondaries that swept through the apparatus from one side to the other, and could be distinguished by the time of flight (TOF) between hodoscope signals in the two arms of the experiment. By using the TOF information it was thus possible to construct a monitor of the SB background.

The procedure for subtracting the background was the following: any measured rate R_{raw} was the sum of a BB contribution $R_{BB} = \sigma L$, and of a background contribution R_{bkg}. If the machine luminosity was varied by changing the beam overlap, this produced a corresponding change in the BB rate, and affected the SB background only slightly. Changes in the background rate were monitored by measuring the rate of the SB monitor R_{SB}:

$$\Delta R_{raw} = \sigma \Delta L + \Delta R_{bkg} = \sigma \Delta L + \beta \Delta R_{SB} \ , \qquad (10)$$

$$\Delta R_{bkg} << \sigma\Delta L \ ,$$

and α and β were obtained by a global fit of the ΔR_{raw} versus ΔL curve. It is clear that this method worked best when i) the background was small, and/or ii) it was not affected by the beam steering.

An example of a TOF spectrum is shown in fig. 7 where events are histogrammed as a function of the time interval between the signals of H_{12L} and H_{12R}. The peak at $\Delta t = 0$ is due to BB interactions; the satellite peaks at positive (negative) intervals are due to SB interactions of beam-1 (beam-2). In the case of this particular TOF, the tails of the three peaks overlap.

Twenty-five $(hod)_L$ - $(hod)_R$ TOFs could, in principle, be computed from the five hodoscope times in each arm, depending on the number of hodoscopes struck in the event. The resolution of the three classes of events (BB, SB_1, SB_2) in different TOFs was a function of the distances of both participating hodoscopes from the crossing point. Accidental firing of the hodoscopes added a flat distribution of events underlying all peaks.

The TOFs (t_i) present in an event were transformed, following Baksay et al. [15], into a set of dimensionless quantities:

$$s_i^2 = (t_i - \langle t_i \rangle)^2 / w_i^2 \ , \qquad (11)$$

where $\langle t_i \rangle$ and w_i were the centre and width of the BB peak in the i^{th} TOF, and were obtained from data taken in clean conditions (pp runs). The widths were 2-6 ns depending on the number of counters in a hodoscope and on their sizes.

The advantage of this transformation lies in the simplicity with which any subset of the 25 TOFs could be summarized in a single number, or super-TOF (STOF), characteristic of the signature of the event:

$$S^2 = \sum_i s_i^2/n \ , \qquad (12)$$

where the sum is performed over the n TOFs in the subset.

It was found convenient to specify five STOFs in the analysis. Their domains of summation are indicated in fig. 8.

The luminosity monitor was derived from the S_M^2 STOF, which was an inclusive STOF: S_M^2 was defined for events in which at least one TOF was present within its domain regardless of the presence of TOFs outside it. Luminosity monitoring and the use of this STOF will be reviewed in subsection 7.2.

Of the remaining STOFs S_a^2 was inclusively defined; S_b^2, $S_{b'}^2$, and S_c^2 were exclusive -- each was defined only in events in which at least one TOF was present within the appropriate domain and no TOFs were present outside. The purpose served by these STOFs will be discussed in detail in subsection 7.4.

As an example of a STOF spectrum let us consider the S_a^2 STOF, which combined the 20 TOFs not involving the CIO_R hodoscope. The distribution of events in S_a^2 is shown in fig. 9 for different beam conditions: a) normal pp running; b) normal $p\bar{p}$ running, with the ISR beams at full vertical overlap (FO); and c) $p\bar{p}$ running with the beams steered apart to almost no overlap (NO). Beam-beam events populate the $S_a^2 < 2$ region, peaking sharply at $S_a^2 = 0$ in the FO spectra. Single-beam events form the broad peaks evident in the $p\bar{p}$ data centred at $S_a^2 \simeq 5$ with tails extending to $S_a^2 = 0$ and $S_a^2 > 10$.

The extreme cleanliness of pp running conditions is demonstrated in fig. 9a.

The residual peak at $S_a^2 = 0$ in the $p\bar{p}$ NO data arises from SB_1 interactions occurring near the interaction zone rather than from BB events, an

interpretation confirmed by reconstructing event vertices with the drift chambers in a sample of $p\bar{p}$ NO data.

The analysis of STOF spectra discussed in subsection 7.3 showed that all of the BB signal was contained in the region $S^2 < 2$ (A region). A small fraction of the total amount of SB background was also found in that region. The part of the spectrum above $S^2 = 2$ (B region) was used to monitor the background [see eq. (10)], both for pp and $p\bar{p}$ measurements.

7.2 Luminosity-monitor calibration

A luminosity monitor ideally combines the following attributes:

i) independence of the precise locations of the beams -- not only because the beams are moved during the calibrations, but also because their size and location generally vary between calibration and data-taking;

ii) large inclusive cross-section -- to accumulate adequate statistics in as short a time as possible; and

iii) insensitivity to background -- for obvious reasons.

Owing to the excellent performance of the ISR, the SB background was virtually negligible with respect to the BB signal during pp running. This remained true even when the beams were separated during the calibrations and the luminosity decreased up to three orders of magnitude on the tails of the VdM curve. It was thus possible to satisfy items (i) , (ii), and (iii) using the entire apparatus as the luminosity monitor. In this way, the luminosity calibration yielded σ_{obs} directly.

This solution could not be adopted for $p\bar{p}$, since SB background from the intense proton beam dominated the full-inclusive trigger. The background was highly asymmetrical, since the SB_1 events fired predominantly the small-angle hodoscopes on the left arm (downstream of the proton beam) and the large-angle hodoscopes on the right arm (CIO_R and H_{12R}). A compromise was therefore reached by choosing an asymmetrical monitor, which was

virtually free of SB background while still presenting an appreciable cross-section:

$$M = (H_5 + H_{34})_L * (H_5 + TB)_R \ . \qquad (13)$$

The inclusivity of this monitor (defined as σ_M/σ_{tot}) varied between 28% and 44%, depending mainly on the c.m. energy.

The monitor calibration [eq. (7)] was done by sampling the luminosity curve, $R_M(\delta)$ versus δ, at a number of values of the beam separation δ, which was adjusted by energizing horizontal-field magnets (H magnets) incorporated in the ISR lattice. At the start of a calibration the beams were steered apart, and then stepped through each other in increments of $\Delta\delta$ = 0.5 or 1.0 mm.

It was found necessary to steer the beams sufficiently far apart to reduce the luminosity to about 0.1% of its full overlap in order to obtain stable values of the monitor cross-section. This is shown in fig. 10, where the measured values of the monitor cross-sections are plotted as a function of the ratio of the luminosity at end-points of the scan to the luminosity at full overlap [the cross-sections in the figure were calculated from a broad scan (27 points with $\Delta\delta$ = 0.5 mm) progressively disregarding end-points]. The monitor-calibration exercises used in this work all satisfied this criterion.

The number of points sampled during typical pp calibrations was 13 (25) for increments of 1.0 (0.5) mm, the entire exercise taking about 1-2 hours. The $p\bar{p}$ calibrations were made with 1.0 mm increments, and required several hours to sample the dozen points needed. About 25,000 events were collected by the data acquisition at each step for off-line analysis.

To minimize instrumental effects, calibrations were performed displacing the beams in I2 only -- and not in all intersections as was the

standard practice. This reduction in the perturbations of the beams gave better accuracy in the beam separation and resulted in less background. For the same reason, the H magnets were cycled prior to calibrations to standardize their magnetic histories, so that precise corrections could be made for hysteresis in the setting of the magnets (Section 4).

In the analysis of calibration data, the true monitor rate was derived from the A- and B-region rates of the monitor STOF [see subsection 7.1]:

$$R_A(\delta) = R_M(\delta) + \beta R_B(\delta) \ . \qquad (14)$$

The signal was represented by a n-parameter function:

$$R_M(\delta) = \exp\left[p_1 - p_2(\delta - p_0)^2 + p_3(\delta - p_0)^3 + \ldots p_{n-1}(\delta - p_0)^{n-1}\right] , \qquad (15)$$

and the parameters β and p_i were extracted from a least-squares fit to the data. Good fits were generally obtained with $n = 6$, where the $n > 3$ parameters expressed the somewhat-faster-than-Gaussian fall-off of luminosity in the tails[3]. The function (15) was then integrated numerically [eq. (7)] to get σ_M. The quality of the data and the fit is apparent in fig. 11, which is taken from the $p\bar{p}$ data at $\sqrt{s} = 52.8$ GeV.

The background subtraction and, in particular, its reliance on the fit for β, were carefully checked. The parameter was an estimate of the ratio of integrated background rates in two regions of the same spectrum, and, as such, is a constant at a particular energy. We checked that values of β obtained in separate calibrations were statistically consistent, and

---

3) The parametrization [eq. (15)] was not unique: a sum of two Gaussians also gave good fits.

the values at a particular setting were averaged. In the final analysis, all calibration data were refitted imposing the average values of β on the fit.

In a small number of $p\bar{p}$ calibrations this check was made more stringent by changing absolute background rates discontinuously during the calibration. Part of the luminosity curve was sampled; background rates were reduced by a factor of about 5, using the scrapers to remove the halo of the proton beam; the remainder of the curve was then sampled. The monitor gave consistent results in all calibrations, including test calibrations of this type.

The monitor M was also calibrated for pp runs, mainly to check for possible systematic differences with respect to $p\bar{p}$. One calibration was performed for pp using asymmetrical beam currents to simulate $p\bar{p}$ conditions; it gave results in agreement with the ones obtained during normal running. Individual measured values of $\sigma_M(p\bar{p})$ and $\sigma_M(pp)$ are listed in table 2 for all calibration runs. (The errors quoted are statistical only and do not include the uncertainty in the beam-displacement scale calibration.)

7.3 The observed pp cross-section

As noted in the preceding subsection, the observed pp cross-section was measured as a part of the luminosity calibration; σ_{obs} was obtained through the same procedure as that followed for σ_M, except that no cuts were made on the STOF spectra to obtain the beam-beam rate; instead, the raw rate of the fully inclusive trigger (R_{tfi}) was used, as it was only slightly contaminated by background. The B region of the S_a^2 distribution (R_B) was used to fit the background [see eqs. (10) and (14)]:

$$R_{tfi}(\delta) = R_{obs}(\delta) + \beta R_B(\delta) \ . \qquad (16)$$

The values of $\sigma_{obs}(pp)$ obtained in individual calibrations are listed in table 3. (The errors are again statistical only.)

To study the effect of cuts in the STOF spectra and to ascertain whether they would introduce systematic biases in the analysis of $p\bar{p}$ data, a parallel analysis for $\sigma_{obs}(pp)$ was conducted by performing on the STOF spectra the same cuts as those applied in the $p\bar{p}$ case. The analysis brought to light only one small effect: in events with few TOFs present, BB events could be displaced from $S^2 < 2$ to $S^2 > 2$ by the out-of-time firing of, usually, a single hodoscope. Such spurious firings resulted from

i) the pile-up of a second event;

ii) back-scattering of secondaries; or

iii) locally induced radioactivity.

The magnitude of the effect was such that was underestimated by 0.2% ($\simeq$ 0.1 mb) in the parallel pp analysis.

Studies with the LED system confirmed these findings. In special runs the LEDs in the trigger hodoscopes were used to reproduce artificially the events that had been previously collected on tape. All the TOFs corresponding to the artificial trigger pattern had to be necessarily in time, hence in the region $S^2 < 2$. Since the tape was replayed when the beams were on, any of the causes (i)-(iii) could displace some of the events beyond the cut. The results showed that less than 0.1% of the events were displaced by TOF misfiring. Since the most significant cause of the effect (i) above was rate-dependent, this figure must be regarded as an upper limit of the corresponding $p\bar{p}$ bias, which could not be measured. No corrections for the cut were therefore applied in the $p\bar{p}$ case.

7.4 The observed $p\bar{p}$ cross-section

In $p\bar{p}$ running conditions, the proton-beam background introduced by the presence of CIO_R in the trigger caused a severe problem. The secondaries

from SB_1 events were emitted in a cone around the p beam, and could easily fire any left-arm hodoscope. The trigger was then satisfied whenever one of the secondaries was produced at a sufficiently wide angle to fire CIO_R, H_{12R}, or -- to a lesser degree -- H_{34R}. The CIO_R hodoscope was so close to the crossing point that TOFs involving it had the same signature for SB_1 events as for BB events. (Similarly, CIO_L TOFs could not distinguish between SB_2 and BB events, but since the $\bar{p}$ beam background was utterly negligible, this was of no consequence.) Moreover, the trigger rate due to cosmic rays was a non-negligible fraction of the BB rate at the low luminosities of $p\bar{p}$ running. These cosmic-ray events were predominantly CIO_L * CIO_R triggers, and, as such, simulated BB events in their TOF signature. The CR trigger rate for other hodoscope combinations was less significant, and such triggers simulated SB events. The five CIO_R TOFs were therefore excluded from consideration in the $p\bar{p}$ analysis, and, for the purpose of measurement, the observed cross-section was broken into three components:

a) interactions firing any of the five left-arm hodoscopes and any of H_{12}, H_{34}, H_5, and TB in the right arm;

b) interactions firing any of H_{12}, H_{34}, H_5, and TB in the left arm, and <u>only</u> CIO in the right arm; and

c) interactions firing <u>only</u> CIO in <u>both</u> arms.

The relative contribution of the components to σ_{obs} was

$$\sigma_a : \sigma_b : \sigma_c :: 0.99 : <0.01 : <0.001 \ ,$$

$$\sigma_{obs} = \sigma_a + \sigma_b + \sigma_c \ . \qquad (17)$$

The dominant component σ_a was measured directly.

To obtain σ_b we exploited the left/right symmetry of the apparatus by defining a further component $\sigma_{b'}$:

b') interactions firing any of H_{12}, H_{34}, H_5, and TB in the right arm and only CIO in the left arm.

Assuming charge-conjugation invariance in $p\bar{p}$ multiparticle production and perfect right-left symmetry in the apparatus, one has $\sigma_b = \sigma_{b'}$. The symmetry of the detector was checked in pp runs by measuring $r = \sigma_b/\sigma_{b'}$ directly. Deviations from the perfect symmetry were taken into account in the $p\bar{p}$ measurement: $\sigma_b(p\bar{p}) = \sigma_{b'}(p\bar{p})\cdot r(pp)$. The tiny contribution σ_c was assumed to be equal to that measured in pp interactions: $\sigma_c(p\bar{p}) = \sigma_c(pp)$.

Measurements of the subcomponents of σ_{obs} were performed through the generation of STOFs within the appropriate domain of summation (see subsection 7.1).

The STOF distributions were divided into A and B regions, and the A-region rate was parametrized as the sum of signal and background [see eq. (10)],

$$R_A = \sigma L + \beta R_B \ , \tag{18}$$

where σ is the corresponding cross-section. The luminosity was derived from the monitor ($L = R_M/\sigma_M$). To solve eq. (18) for σ and β, two runs were taken: one with the beams fully overlapping (FO); one with beams separated by 4 mm (NO). This yielded a pair of simultaneous equations in two unknowns:

$$\begin{aligned} R_A^{FO} &= \alpha R_M^{FO} + \beta R_B^{FO} \ , \\ R_A^{NO} &= \alpha R_M^{NO} + \beta R_B^{NO} \ , \end{aligned} \tag{19}$$

where $\sigma = \alpha\sigma_M$. The duration of such runs was kept short ($\lesssim$ 15 min), and the beam separation was accomplished by moving the $\bar{p}$ beam but not the p beam. These precautions were taken to minimize changes in the characteristics (not necessarily in the rate) of the background. Many ($\lesssim$ 30) pairs of runs were taken, and the final values of α were obtained by averaging. A set of measurements for α is presented in fig. 12 ($\sqrt{s}$ = 52.8 GeV).

We checked that the method was insensitive to absolute background rates by reducing them discontinuously (in the same way as in the luminosity calibrations) between one pair of runs and another; β of course changed, but α was constant within the statistical accuracy.

The individual contributions to $\sigma_{obs}(p\bar{p})$ are summarized in table 4 (the errors are statistical only).

7.5 Elastic-loss correction term

The fraction of elastic interactions that escaped detection owing to the small-angle holes in the apparatus was estimated by a Monte Carlo (MC).

In the MC, the finite extent of the interaction zone was re-created from the measured radial profile of the ISR beams (Schottky scan) and, in the vertical direction, from the width of the luminosity curve. The differential elastic cross-section (fig. 13) was used to generate elastic-scattering events, and was parametrized as an exponential in the momentum-transfer squared (t), allowing for a change in the slope parameter at $|t_{ch}| = 0.15\ (\mathrm{GeV}/c)^2$:

$$d\sigma_{el}/d\Omega = (d\sigma_{el}/d\Omega)_0 \exp(bt)\ ,$$

$$b = b_1\ ; \quad |t| < |t_{ch}|\ , \tag{20}$$

$$b = b_2\ ; \quad |t| > |t_{ch}|\ .$$

Normalization was achieved via the optical theorem

$$(d\sigma_{el}/d\Omega)_0 = \sigma_{tot}^2 p_{ISR}^2 (1 + \varrho^2)/16\pi^2 \ , \qquad (21)$$

where ϱ is the ratio of the real to the imaginary part of the forward nuclear scattering amplitude. With this normalization the correction term was found to be independent to first approximation of the precise form (b_1, b_2, t_{ch}) of the angular dependence. The values used for b_1, b_2 are shown in table 5.

In the energy range of interest, the ratio ϱ was about 0.1; it therefore had little effect on the correction term. The values used were taken from Amaldi and Schubert [16] for pp and from Amos et al. [20] for $p\bar{p}$.

To obtain the correction term, eq. (20) was integrated over the solid angle subtended by the TB holes. No account was taken of secondary interactions:

$$\Delta\sigma_{el} = (d\sigma_{el}/d\Omega)_0 \int_{mc} \exp(bt)\, d\Omega \ . \qquad (22)$$

This definition of $\Delta\sigma_{el}$ was recursive, since it contained the value of σ_{tot} [eq. (21)], and the values of the correction term were calculated iteratively.

At $\sqrt{s}$ = 30.6 GeV, the correction includes a term to compensate for the Coulomb scattering [at this energy, the minimum angle subtended by the trigger in the vertical plane (3.2 mrad) corresponded to $|t| = 0.0025$ $(GeV/c)^2$]. The increase of the measured cross-section computed using the known Coulomb cross-section as an input, amounted to 0.00 (0.07) mb for pp ($p\bar{p}$) and was completely negligible at the higher energies.

The correction terms are listed in table 6. The errors in $\Delta\sigma_{el}$ arise from uncertainties in the input parameters, and were estimated by variation

of these parameters. The dominant uncertainty was that associated with the transverse dimensions of the TB holes. We therefore treated the error in $\Delta\sigma_{el}$ as a systematic one.

7.6 Inelastic-loss correction term

The cross-section loss due to the non-detection of inelastic-scattering events was calculated by extrapolating an angular distribution and performing a MC integration over the uncovered region, in a manner analogous to that used for the elastic loss. The angular distribution used was established empirically from the data.

A clean sample of events was prepared by rejecting background events at $S_a^2 > 1$. Track information for the event was given by the θ hodoscopes. Elastic-scattering events were removed from the sample by requiring a hit at $\theta > 40$ mrad in one arm. For the remaining events, the widest-angle track (θ_{max}) was found in the opposite arm and the inclusive distribution $dN/d\Omega_{max}$ was obtained. We found that at small θ_{max} the distribution was exponential in the variable $t' = -2\, p_{ISR}^2\, (1 - \cos\theta_{max})$ (fig. 14) with a slope parameter of the order of half that found for elastic-scattering interactions. Normalization of this cross-section was obtained through the luminosity monitors:

$$\Delta\sigma_{in} = (\sigma_M/N_M) \int_{mc} (dN/d\Omega_{max})\, d\Omega_{max} ,$$

$$dN/d\Omega_{max} = N_0 \exp(ct') . \qquad (23)$$

The values of $\Delta\sigma_{in}$ are listed in table 6. As in the case of the elastic loss, the error quoted is systematic and dominated by the uncertainty in the transverse dimensions of the TB holes.

7.7 Other correction terms

It has been argued [35] that at sufficiently high energies, inelastic electromagnetic amplitudes may compete with or even dominate [36] certain nuclear ones. The leading e.m. diagram is single-photon exchange resulting in the diffractive excitation of one of the incident particles. This contribution to pp → pX has been calculated [36] and amounts to $\sigma_{em}(pp \to pX) \simeq$ 0.1 mb at the highest ISR energy, when the excitation of both protons is taken into account. The purely electromagnetic process is thus almost negligible at the ISR, in comparison with nuclear processes.

The similarity of diffractive excitation proceeding through photon exchange and Pomeron exchange, however, is such that there may be appreciable interference between the two amplitudes.

We tried to estimate the order of magnitude of this effect, assuming that the e.m. nuclear excitation proceeds with an amplitude similar to the purely hadronic diffraction dissociation. We also assumed that the phases of the two amplitudes were the same as those for the elastic processes [37].

Under these assumptions we obtained for the interference contribution,

$$\sigma_{int}(pp \to pX) \simeq -0.2 \text{ mb} ,$$

at the highest ISR energy.

Although larger than the pure e.m. term, the interference term is still relatively unimportant in comparison with inelastic nuclear processes, assuming that the above assumptions are correct.

Where the e.m. effect could become important is in the cross-section difference, $\Delta\sigma_{tot} = \sigma_{tot}(p\bar{p}) - \sigma_{tot}(pp)$. The sign of the e.m. amplitude in $p\bar{p}$ reactions is reversed with respect to the corresponding pp one. The

contribution of the interference term to the cross-section difference could be then as large as $\sigma_{int} = 0.4$ mb, and by no means unimportant in comparison with the nuclear contribution to the difference.

Hampered by our lack of knowledge of strong amplitudes, we did not, however, attempt to refine our estimate of inelastic e.m. effects or to correct the cross-section for such effects.

8. CONCLUSIONS

8.1 Total cross-section results

The total cross-section results on proton-proton and proton-antiproton reactions are listed in table 6. Contributions to the errors arise from statistics and from systematics, the geometry of the TB holes being the dominant instrumental effect. Errors from different sources have been combined in quadrature in the final result.

The present measurements of the proton-proton total cross-section are the most precise among similar measurements performed at the ISR. In fig. 15 our proton-proton measurements are compared with those performed earlier at the ISR [15], with the average values thereof computed by Amaldi and Schubert [16] and with the recent measurements of Amos et al. [10]. Where scale errors were quoted separately, in the figure they have been combined in quadrature with the point-to-point errors. At $\sqrt{s} = 30.6$ GeV the agreement among the measurements is excellent. Our results become higher than the Amaldi and Schubert average with increasing energy, but still remain statistically well compatible.

We have investigated whether the two experimental methods used to measure the total cross-section (total rate and optical-theorem methods) might have led to systematically different results, being, in principle, affected by different systematic effects. Our conclusions are, that within the precision of the measurements, no statistically significant discrepancy is evident [38].

The proton-antiproton measurements confirm the expectation of a rise in the total cross-section. In the interval $\sqrt{s}$ = 30.6 to 62.7 GeV the $p\bar{p}$ cross-section rises by 2.34 $\pm$ 0.64 mb, whereas for the pp cross-section the increase is 3.60 $\pm$ 0.35 mb. The two cross-sections are therefore both rising and approaching each other, following the universal trend of total hadronic cross-sections which is apparent from fig. 16. The solid lines in fig. 16 were computed according to the 'universal' parametrization of Lipkin [39], and are shown mainly to guide the eye.

The total cross-section differences $\Delta\sigma_{tot} = \sigma_{tot}(p\bar{p}) - \sigma_{tot}(pp)$ are listed in table 7. In the calculation of the difference, some systematic uncertainties cancel, and this is reflected in the errors, which include both the point-to-point and the energy-independent errors. The cross-section differences are plotted in fig. 17, together with other lower-energy data; $\Delta\sigma_{tot}$ decreases smoothly with the energy, following the trend of lower-energy measurements.

Regge phenomenology predicts that the decrease should obey a power-law dependence on the energy [40]. In the Regge picture, the leading Pomeron contribution, even under C, cancels in the difference, and the behaviour is predicted to be $s^{-1/2}$ owing to the dominance of the ϱ and ω trajectories. The fit in fig. 17 (see also subsection 8.2) yields $\Delta\sigma \propto s^{-(0.57\pm0.01)}$, and it is obviously dominated from the low-energy data; our measurements (and possibly the highest-energy FNAL data) suggest a small, systematic deviation above this power-law extrapolation from lower energy, but this cannot be taken as an indication of a departure from the Regge-exchange picture. As we pointed out in subsection 7.7, there is the possibility that a small but significant inelastic e.m. contribution is incorporated in the difference. It is interesting to remark, in this respect, that the points of Amos et al. [10] (obtained by exploiting the optical theorem and

therefore free from this e.m. contribution) seem to fit the Regge behaviour better.

8.2 Behaviour of σ_{tot} as a function of s

Figure 18 shows a compilation [41-43] of total cross-sections for $p\bar{p}$ and pp interactions over the energy range covered today. In addition to the slow approach of the two cross-sections at high energy, we remark the approximately parabolic shape as a function of ln s, which suggests that the asymptotic trend is

$$\sigma_{tot} \propto \ln^2 s \ .$$

This type of asymptotic energy dependence was actually foreseen long ago by Heisenberg [44] in an optical-model framework. The same behaviour was predicted several years later by Cheng and Wu [8] using a field-theoretical approach. The $\ln^2 s$ behaviour is the fastest one allowed by the Froissart bound.

In order to find a simple interpolating formula that represents the $p\bar{p}$ and pp data, we have fitted the data in the energy range $\sqrt{s}$ = 4 to 62.7 GeV, assuming that $\sigma_{tot}(pp)$ is built up of two terms: a constant plus a power of of $|\ln s|$ to account for the asymptotic rise. The difference $\Delta\sigma_{tot} = \sigma_{tot}(p\bar{p}) - \sigma_{tot}(pp)$ has been parametrized by a Regge-like term, s^{-C}. Proton-proton and proton-antiproton data have been fitted simultaneously, and the results are (σ's are in mb, s is in GeV^2):

$$\sigma_{tot}(pp) = (38.31 \pm 0.02) + (0.545 \pm 0.02)\ |\ln (s/122 \pm 2)|^{1.89 \pm 0.04} \ ,$$

$$\Delta\sigma_{tot} = (77 \pm 4)\ s^{-0.57 \pm 0.01} \ ,$$

$$\chi^2/DOF = 95/79 .$$

The fit is shown in fig. 16. This parametrization fits the data well up to the SPS Collider energy.

Acknowledgements

The experiment was made possible by the combined achievement of the staffs of the PS, the AA, and the ISR. The success of the experiment, linked so intimately to the machine at which it was performed, was due in large part to the excellence and dedication of the ISR operations team.

The skill and zeal of G. Barnini, A. Bechini, A. Donnini, L. Giacomelli and T. Regan, and of the technical staff of the University of Naples, were gratefully appreciated during all stages of the experiment.

We also thank Mme R. Dubos-Latrauguere for her patient administrative assistance during the course of the experiment.

REFERENCES

[1] For a review of high-energy theorems and developments in the field, see R.J. Eden, Rev. Mod. Phys. 43 (1971) 15.
S.M. Roy, Phys. Rep. 5 (1972) 125.
J. Fischer, Phys. Rep. 76 (1981) 1572.

[2] I.Ya. Pomeranchuk, Zh. Eksp. Teor. Fis. 34 (1958) 25 [translated in Sov. Phys.-JETP 7 (1958) 499].

[3] M. Froissart, Phys. Rev. 123 (1961) 1053.

[4] For a discussion of this and other aspects of high-energy scattering, see: G. Giacomelli, Phys. Rep. 23 (1976) 123.
G. Alberi and G. Goggi, Phys. Rep. 74 (1981) 1.
K. Goulianos, Phys. Rep. 101 (1983) 169.

[5] For a review of models current at that time, see: F. Zachariasen, Phys. Rep. 2 (1971) 1.

[6] For example: V. Barger, M. Olsson and D.D. Reeder, Nucl. Phys. B5 (1968) 411.
S. Frautschi and B. Margolis, Nuovo Cimento 56A (1968) 1155.
V.N. Gribov and A.A. Migdal, Yad. Fiz. 8 (1968) 1213 [translated in Sov. J. Nucl. Phys. 8 (1969) 703].

[7] For example: N. Cabibbo et al., Nuovo Cimento 45A (1966) 275.
H. Cheng and T.T. Wu, Phys. Rev. Lett. 22 (1969) 1405.

[8] For example: H. Cheng and T.T. Wu, Phys. Rev. Lett. 24 (1970) 1456.
S.J. Chang and T.M. Yan, Phys. Rev. Lett. 25 (1970) 1586.

[9] Total-cross-section measurements at the BNL Alternating Gradient Synchrotron:
W. Galbraith et al., Phys. Rev. 138 (1965) B913.
A. Citron et al., Phys. Rev. 144 (1966) 1101.
K.J. Foley et al., Phys. Rev. Lett. 19 (1967) 330 and 857.

[10] Total-cross-section measurements at the IHEP proton synchrotron:
J.V. Allaby et al., Phys. Lett. 30B (1969) 500.
S.P. Denisov et al., Phys. Lett. 36B (1971) 415 and 528.
Yu.B. Bushnin et al., Yad. Fiz. 16 (1972) 1224 [translated in Sov. J. Nucl. Phys. 16 (1973) 675].
S.P. Denisov et al., Nucl. Phys. B65 (1973) 1.

[11] U. Amaldi et al., Phys. Lett. 44B (1973) 112.

[12] S.R. Amendolia et al., Phys. Lett. 44B (1973) 119.

[13] G.B. Yodh, Yash Pal and J.S. Trefil, Phys. Rev. Lett. 28 (1972) 1005.

[14] U. Amaldi et al., Phys. Lett. 66B (1977) 390.

[15] Earlier total-cross-section measurements at the CERN ISR:
K. Eggert et al., Nucl. Phys. B98 (1975) 93.
L. Baksay et al., Nucl. Phys. B141 (1978) 1.
U. Amaldi et al., Nucl. Phys. B145 (1978) 367.

[16] U. Amaldi and K.R. Schubert, Nucl. Phys. B166 (1980) 301.

[17] Total-cross-section measurements at the FNAL proton synchrotron:
D. Bogert et al., Phys. Rev. Lett. 20 (1973) 1271.
A.S. Carroll et al., Phys. Rev. Lett. 33 (1974) 928 and Phys. Lett. 61B (1976) 303.
A. Firestone et al., Phys. Rev. D14 (1976) 2902.
A.S. Carroll et al., Phys. Lett. 80B (1979) 423.

[18] A. Breakstone et al., Phys. Lett. 114B (1982) 383.
A.L.S. Angelis et al., Phys. Lett. 118B (1982) 217.
T. Åkesson et al., Phys. Lett. 121B (1983) 439 and 129B (1983) 269.
A. Breakstone et al., Phys. Lett. 132B (1983) 458.

[19] T. Åkesson et al., Phys. Lett. 108B (1982) 58.

P. Chauvat et al., Phys. Lett. 127B (1983) 384.

T. Åkesson et al., Nucl. Phys. B228 (1983) 409.

V. Cavasinni et al., Z. Phys. C21 (1984) 299.

A. Breakstone et al., preprint CERN/EP 84-105 (1984).

S. Erhan et al., preprint CERN/EP 84-147 (1984).

[20] D. Favart et al., Phys. Rev. Lett. 47 (1981) 1191.

N. Amos et al., Phys. Lett. 120B (1983) 460 and 128B (1983) 343.

[21] G. Carboni et al., Phys. Lett. 108B (1982) 145 and 113B (1982) 87.

M. Ambrosio et al., Phys. Lett. 115B (1982) 495.

[22] K. Johnsen, The possibility of p + $\bar{p}$ colliding beam experiments in a set of storage rings, CERN internal report AR/Int. SG/62-11 (1962).

[23] S. van der Meer, Filling the ISR with antiprotons from hyperon decay, CERN divisional report ISR-PO/70-5 (1970).

K. Hübner, The storage of antiprotons in the ISR, CERN divisional report ISR-TH/73-19 (1973).

K. Hübner, K. Johnsen and G. Kantardjian, The feasibility of antiprotons in the ISR, CERN divisional report ISR-LTD/75-45 (1975).

P.J. Bryant, IEEE Trans. Nucl. Sci. NS-26 (1979) 3234.

[24] G.I. Budker, in Proc. Int. Symp. on Electron and Positron Storage Rings, Saclay, 1966 (eds. H. Zyngier and E. Crémieu-Alcan (Presses Universitaires de France, Paris, 1966), p. II-1-1.

S. van der Meer, Stochastic damping of betatron oscillations in the ISR, CERN divisional report ISR-PO/72-31 (1972).

See also: D. Möhl et al., Phys. Rep. 58 (1980) 73.

F.T. Cole and F.E. Mills, Annu. Rev. Nucl. Part. Sci. 31 (1981) 295.

[25] R. Billinge and M.C. Crowley-Milling, IEEE Trans. Nucl. Sci. NS-26 (1979) 2974.

[26] The PS Staff, The CERN PS complex: A multipurpose particle source, CERN divisional report PS/83-26 (1983).

[27] K.M. Terwilliger, Proc. Int. Conf. on High-Energy Accelerators and Instrumentation, Geneva, 1959, ed. L. Kowarski (CERN, Geneva, 1959), p. 53.

P.J. Bryant, IEEE Trans. Nucl. Sci. NS-20 (1973) 773.

[28] P. Bryant et al., IEEE Trans. Nucl. Sci. NS-20 (1973) 799.

[29] K. Unser, IEEE Trans. Nucl. Sci. NS-16 (1969) 934.

[30] S.R. Amendolia et al., Nuovo Cimento 17A (1973) 735.

[31] S. van der Meer, Calibration of the effective beam height in the ISR, CERN internal report ISR-PO/68-31 (1968).

[32] K. Potter and S. Turner, IEEE Trans. Nucl. Sci. NS-22 (1975) 1589.

[33] P. Bryant and K. Potter, CERN internal report, CERN-ISR-ES-BOM/82-15 (1982).

[34] A. Bechini et al., Nucl. Instrum. Methods 156 (1978) 181.

[35] S.M. Berman and S.D. Drell, Phys. Rev. 133 (1964) B791.

S.M. Berman, J.D. Bjorken and J. Kogut, Phys. Rev. D4 (1971) 3388.

F.E. Low and S.B. Treiman, Phys. Rev. D5 (1972) 756.

[36] G. Berlad et al., Ann. Phys. (USA) 75 (1973) 461.

[37] M.P. Locher, Nucl. Phys. B2 (1967) 525.

G.B. West and D.R. Yennie, Phys. Rev. 172 (1968) 1413.

[38] T. Del Prete, Proc. Moriond Workshop on Antiproton-Proton Physics and the W Discovery, La Plagne, 1983 (Ed. Frontières, Gif-sur-Yvette, 1984) p. 49.

[39] H.J. Lipkin, Phys. Rev. D11 (1975) 1827.

[40] For a discussion of this and other aspects of particle-antiparticle reaction differences, see J.G. Rushbrooke and B.R. Webber, Phys. Rep. 44 (1978) 1.

[41] V.D. Bugg, Phys. Rev. 146 (1966) 980.

[42] G. Arnison et al., Phys. Lett. 128B (1983) 336.

[43] R. Battiston et al., Phys. Lett. 117B (1982) 126.

M. Bozzo et al., Phys. Lett. 147B (1984) 392.

[44] W. Heisenberg, Kosmische Strahlung (Springer Verlag, 1953), p. 148.

Table 1

Details of $p\bar{p}$ runs

$\sqrt{s}$ (GeV)	I_1 (A)	I_2 (mA)
30.6	9.71	4.18
"	5.09	4.09
"	11.02	4.06
52.8	10.33	1.99
"	10.30	1.99
"	6.42	1.95
"	9.04	1.92
62.7	11.84	2.02
"	9.26	3.35
"	9.14	3.17

Note: the currents listed were those at the beginning of the run

Table 2

Individual measured values of the cross-section of the monitor $M = (H_5 + H_{34})_L * (H_5 + TB)_R$.

(The errors are statistical only.)

$\sqrt{s}$ (GeV)	$\sigma_M(pp)$ (mb)	$\sigma_M(p\bar{p})$ (mb)
30.6	11.16 ± 0.05 11.19 ± 0.05 11.09 ± 0.05	12.22 ± 0.06 12.05 ± 0.09 12.09 ± 0.04
(avg)	11.15 ± 0.03	12.12 ± 0.03
52.8	17.42 ± 0.09 17.18 ± 0.17 17.16 ± 0.10 17.24 ± 0.07 17.25 ± 0.06 17.26 ± 0.06 17.53 ± 0.08 17.68 ± 0.07	17.85 ± 0.20 18.45 ± 0.12 18.77 ± 0.12 18.54 ± 0.08
(avg)	17.36 ± 0.03	18.51 ± 0.06
62.7	18.80 ± 0.06 19.36 ± 0.06 19.00 ± 0.07 19.10 ± 0.06 19.13 ± 0.08	18.01 ± 0.08 18.39 ± 0.06 18.12 ± 0.08
(avg)	19.08 ± 0.03	18.21 ± 0.04

Table 3

Individual measured values of the cross-section of the fully inclusive trigger $\sigma_{obs}(pp)$. Values of the beam currents are also given. (The errors are statistical only.)

$\sqrt{s}$ (GeV)	$\sigma_{obs}(pp)$ (mb)	I_1 (A)	I_2 (A)
30.6	39.35 ± 0.10	6.82	6.75
	39.43 ± 0.10	5.50	5.55
	39.38 ± 0.09	5.04	5.08
(avg)	39.39 ± 0.06		
52.8	40.77 ± 0.13	10.43	10.32
	40.09 ± 1.29	10.43	5.1×10^{-3}
	40.30 ± 0.15	2.15	2.22
	40.60 ± 0.10	2.15	2.22
	40.51 ± 0.10	3.46	3.52
	40.60 ± 0.10	3.46	3.52
	40.90 ± 0.12	3.46	3.52
	41.13 ± 0.11	1.04	1.02
(avg)	40.70 ± 0.04		
62.7	40.44 ± 0.09	5.62	5.30
	41.24 ± 0.09	4.19	4.50
	40.55 ± 0.14	2.71	2.70
	40.87 ± 0.09	2.67	2.50
	40.69 ± 0.12	2.65	2.46
(avg)	40.80 ± 0.05		

Table 4

Measured components of the $p\bar{p}$ observed cross-section,

$\sigma_{obs} = \sigma_a + \sigma_b + \sigma_c$. (The errors are statistical only.)

$\sqrt{s}$ (GeV)	σ_a (mb)	σ_b (mb)	σ_c (mb)	σ_{obs} (mb)
30.6	41.38 ± 0.26	0.47 ± 0.03	0.03 ± 0.01	41.89 ± 0.26
52.8	42.02 ± 0.31	0.22 ± 0.03	0.03 ± 0.01	42.27 ± 0.32
62.7	41.70 ± 0.19	0.24 ± 0.02	0.03 ± 0.01	41.97 ± 0.19

Table 5

The slopes of the differential elastic cross-section

used in the calculation of the elastic losses

$\sqrt{s}$ (GeV)	b_1 (GeV^{-2})		b_2 (GeV^{-2})	
	pp	$p\bar{p}$	pp	$p\bar{p}$
30.6	12.2 ± 0.2 a)	12.2 ± 0.2 d)	10.9 ± 0.2 a)	10.9 ± 0.2 d)
52.8	13.1 ± 0.4 b)	13.9 ± 0.4 b)	10.3 ± 0.2 b)	10.7 ± 0.2 b)
62.7	13.3 ± 0.2 a)	13.1 ± 0.6 c)	10.4 ± 0.2 a)	10.4 ± 0.2 d)

a) U. Amaldi et al., ref. 15
b) M. Ambrosio et al., ref. 21
c) N. Amos et al., ref. 20
d) pp value used for $p\bar{p}$

Table 6

The final pp and $p\bar{p}$ results: $\sigma_{tot} = \sigma_{obs} + \Delta\sigma_{el} + \Delta\sigma_{in}$.

Reaction	$\sqrt{s}$ (GeV)	σ_{obs} a) (mb)	$\Delta\sigma_{el}$ b) (mb)	$\Delta\sigma_{in}$ b) (mb)	σ_{tot} c) (mb)
pp	30.6	39.39 ± 0.06 ± 0.16	0.60 ± 0.00 ± 0.03	0.23 ± 0.01 ± 0.01	40.22 ± 0.21
pp	52.8	40.70 ± 0.04 ± 0.17	1.80 ± 0.00 ± 0.07	0.51 ± 0.01 ± 0.01	43.01 ± 0.27
pp	62.7	40.80 ± 0.05 ± 0.17	2.42 ± 0.00 ± 0.09	0.60 ± 0.01 ± 0.01	43.82 ± 0.30
$p\bar{p}$	30.6	41.89 ± 0.26 ± 0.17	0.68 ± 0.00 ± 0.03	0.24 ± 0.01 ± 0.01	42.80 ± 0.35
$p\bar{p}$	52.8	42.27 ± 0.31 ± 0.17	1.92 ± 0.00 ± 0.08	0.52 ± 0.03 ± 0.01	44.71 ± 0.46
$p\bar{p}$	62.7	41.97 ± 0.19 ± 0.17	2.54 ± 0.00 ± 0.09	0.64 ± 0.03 ± 0.02	45.14 ± 0.38

a) The first error quoted is statistical; the second is the error arising from the calibration of the beam-displacement scale.
b) The first error is statistical; the second is systematic.
c) The error is the combination of all errors in the components.

Table 7

The difference between the $p\bar{p}$ and pp total cross-sections (the systematic errors in the corrective terms, $\Delta\sigma_{el}$ and $\Delta\sigma_{in}$, have not been included, see text)

$\sqrt{s}$ (GeV)	$\Delta\sigma_{tot}$ (mb)
30.6	2.58 ± 0.41
52.8	1.70 ± 0.53
62.7	1.32 ± 0.48

Figure captions

Fig. 1 : Plan view of the CERN antiproton complex.

Fig. 2 : Profile in time of the antiproton current during an ISR $p\bar{p}$ run.

Fig. 3 : Zero-prong topological cross-section for $p\bar{p}$ interactions extrapolated to the ISR energy range.

Fig. 4 : Layout of scrapers and pick-ups around Intersection 2.

Fig. 5 : The difference between scraper measurements (z_m) and nominal beam position (z_s) as a function of z_s. The slope of the fitted straight line is the average error in the beam displacements.

Fig. 6 : Layout of the experimental apparatus. Antiprotons circulated in Beam 2. The inset shows an exploded view of the TB hodoscopes equipped with the elastic-scattering detector (TBy: scintillator hodoscope; TBz: drift tubes).

Fig. 7 : Example of a TOF spectrum ($H_{12L} - H_{12R}$). The distribution was taken from a pp run with the ISR beams scarcely overlapping in order to enhance the background.

Fig. 8 : Domains of summation of the various super-TOFs used in the analysis.

Fig. 9 : Distribution of the events in the variable S_a^2 combining 20 left-right TOFs: a) pp data with overlapping beams; b) $p\bar{p}$ data with overlapping beams; and c) $p\bar{p}$ data with the beams steered 4 mm apart. Normalization is as follows: (a) and (b) correspond to the same integrated luminosity, and (b) and (c) correspond to the same live-time.

Fig. 10 : Stability of the measured value of the monitor cross-section as a function of the span of the measurement.

Fig. 11 : Luminosity curve taken from a $p\bar{p}$ monitor calibration at $\sqrt{s}$ = 52.8 GeV.

Fig. 12 : Measured values of the parameters $\alpha_a = \sigma_a/\sigma_M$ and $\alpha_b = \sigma_b/\sigma_M$ taken from $p\bar{p}$ data at $\sqrt{s}$ = 52.8 GeV.

Fig. 13 : Differential elastic cross-sections for $p\bar{p}$ and pp scattering at $\sqrt{s}$ = 52.8 GeV measured in this apparatus (Ambrosio et al. [21]).

Fig. 14 : Distribution of the single-diffractive events in $|t'|$ (see text) for a) pp and b) $p\bar{p}$ scattering at $\sqrt{s}$ = 52.8 GeV.

Fig. 15 : Comparison of our $\sigma_{tot}(pp)$ measurements with other ISR measurements. Values indicated with open symbols were obtained from the extrapolated forward elastic cross-section via the optical theorem. The solid symbols denote the values obtained from the total-rate method.

Fig. 16 : Compilation of hadron-proton total cross-sections. The data were taken from this experiment and from refs. 9 [AGS], 10 [IHEP], 17 [FNAL], 16 [ISR pp], and 20 [ISR, $p\bar{p}$]. The curves were computed according to Lipkin's parametrization (see text).

Fig. 17 : Compilation of $p\bar{p}$ - pp total cross-section differences. The data were taken from this experiment and from refs. 10 [IHEP], 17 [FNAL], and 20 [ISR]. The straight line is a fit assuming Regge behaviour of the difference (see text).

Fig. 18 : Compilation of results on the $p\bar{p}$ and pp total cross-sections. The solid lines correspond to the fit to the data discussed in the text. The compilation comprises low-energy data [41] and SPS Collider data [42,43].

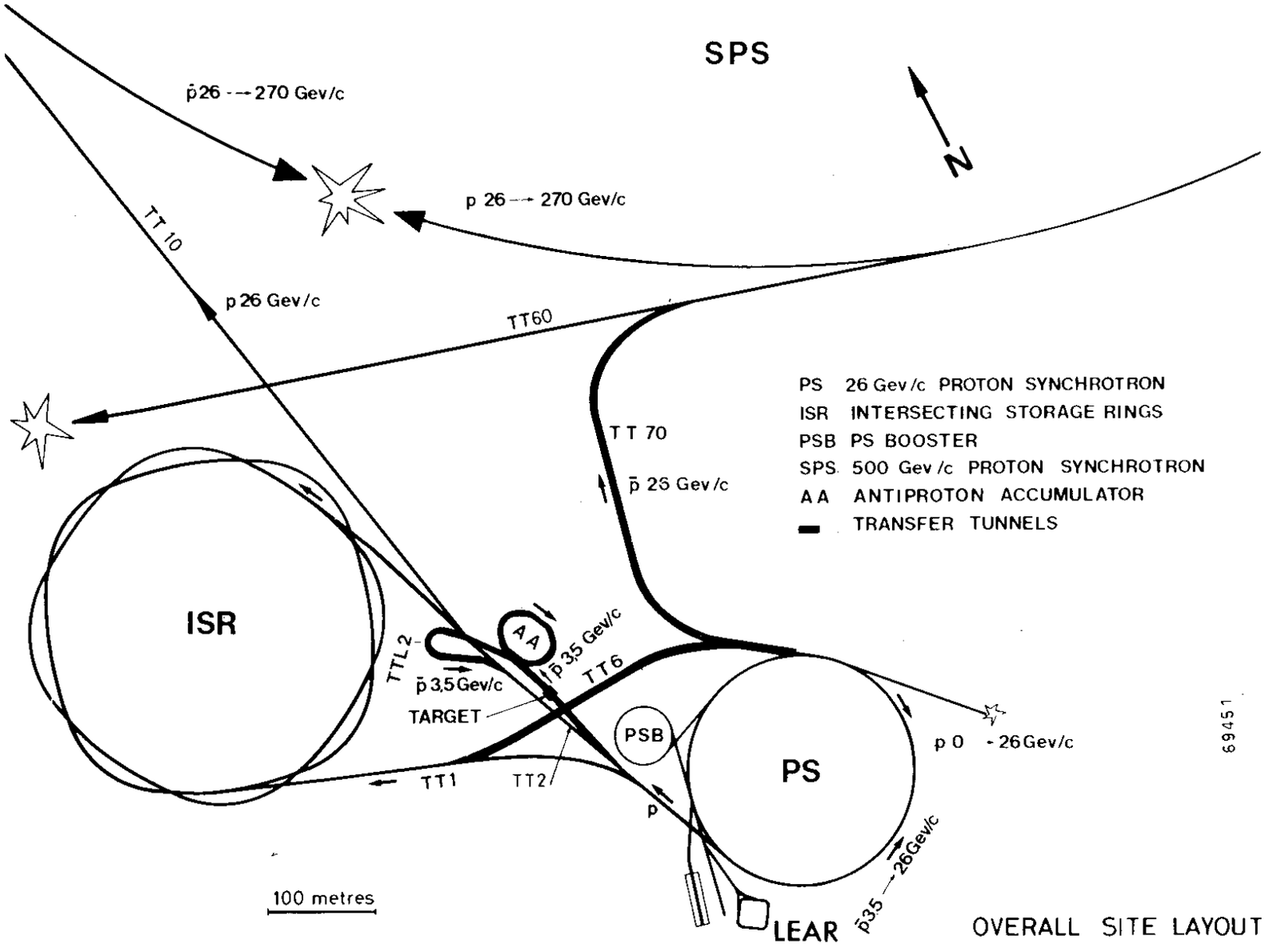
SPS
p̄ 26 → 270 Gev/c
p 26 → 270 Gev/c
N
TT 10
p 26 Gev/c
TT60
TT 70
p̄ 26 Gev/c
PS 26 Gev/c PROTON SYNCHROTRON
ISR INTERSECTING STORAGE RINGS
PSB PS BOOSTER
SPS 500 Gev/c PROTON SYNCHROTRON
AA ANTIPROTON ACCUMULATOR
TRANSFER TUNNELS
ISR
TTL2
AA
p̄ 3,5 Gev/c
TT6
p̄ 3,5 Gev/c
TARGET
PSB
PS
p 0 - 26 Gev/c
TT1
TT2
p
p̄ 3,5 — 26 Gev/c
LEAR
100 metres
OVERALL SITE LAYOUT
69451

Fig. 1

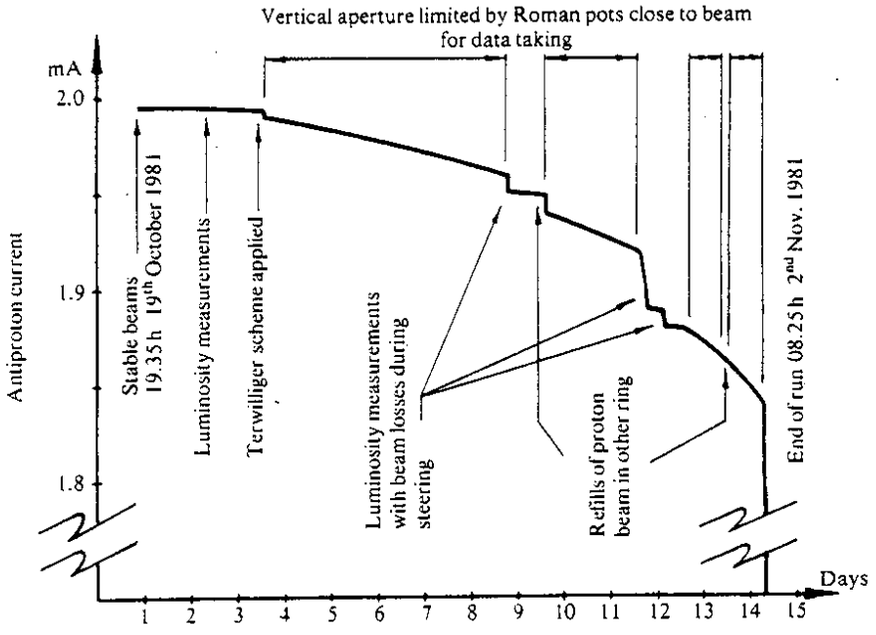
Vertical aperture limited by Roman pots close to beam for data taking
mA
2.0
1.9
1.8
Antiproton current
Stable beams 19.35 h 19th October 1981
Luminosity measurements
Terwilliger scheme applied
Luminosity measurements with beam losses during steering
Refills of proton beam in other ring
End of run 08.25 h 2nd Nov. 1981
Days
1 2 3 4 5 6 7 8 9 10 11 12 13 14 15

Fig. 2

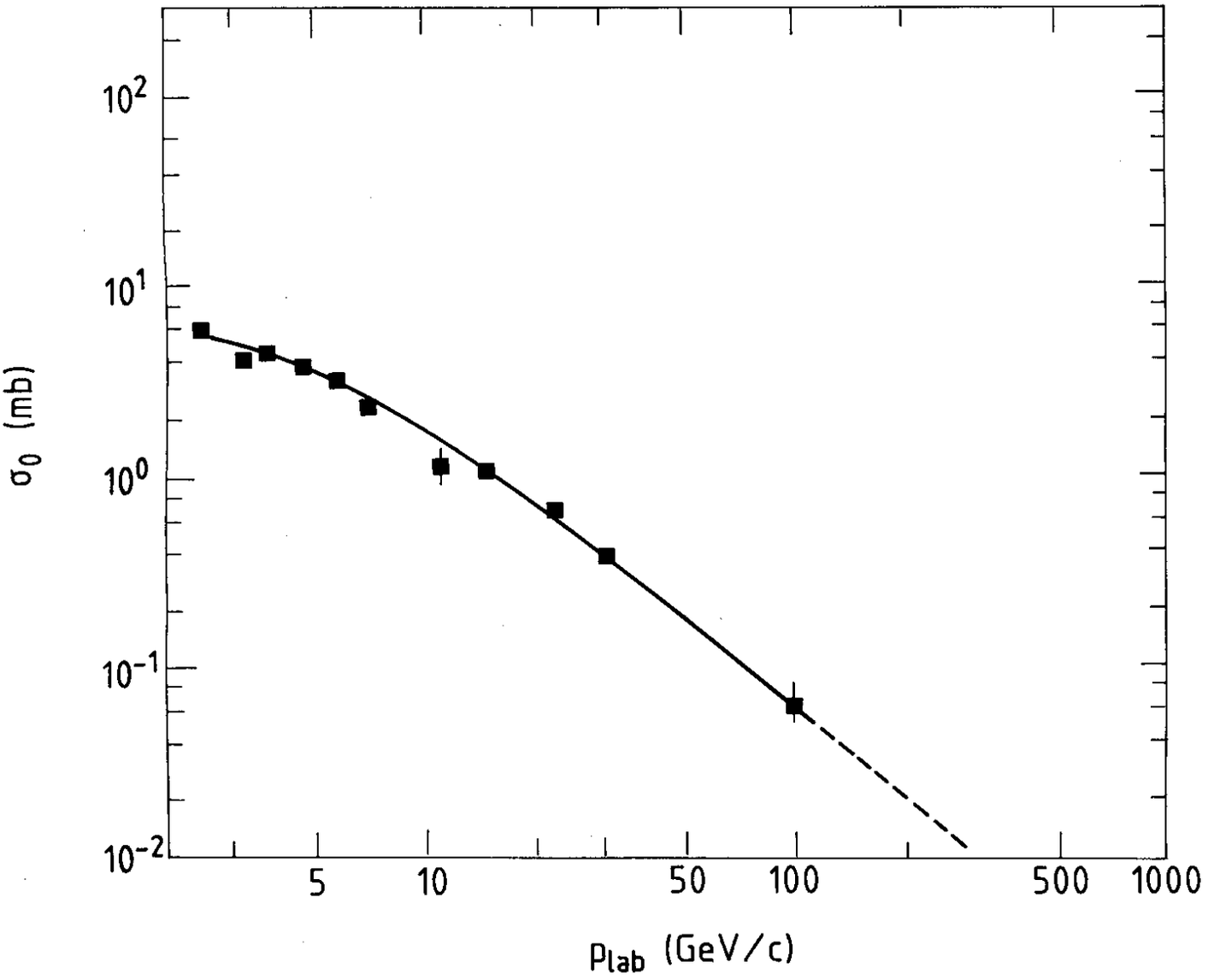

Fig. 3

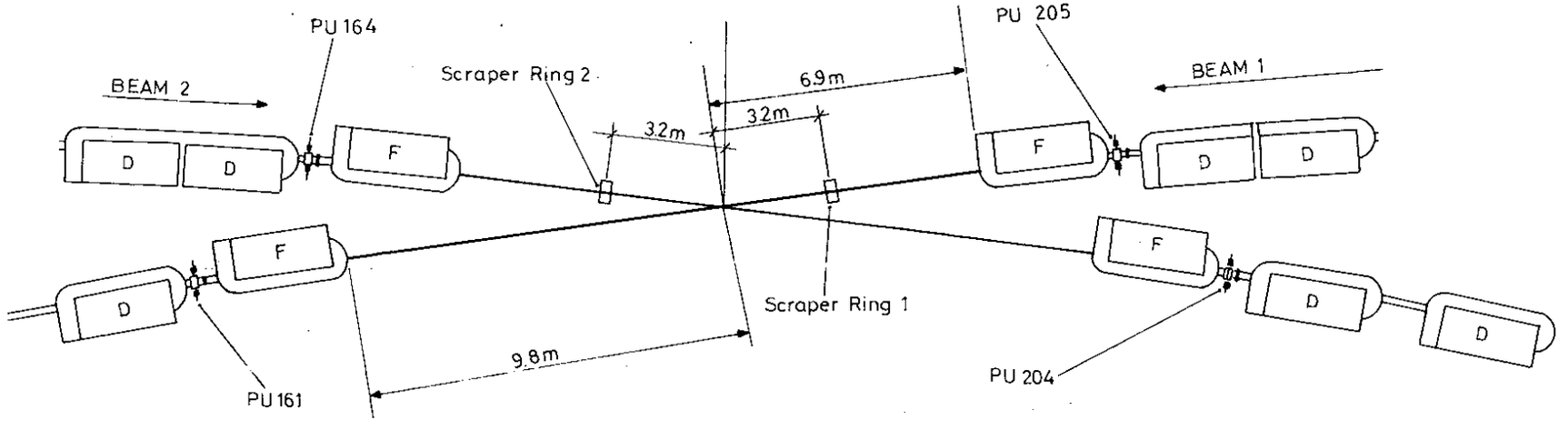
PU 164
PU 205
BEAM 2
BEAM 1
Scraper Ring 2
6.9m
3.2m
3.2m
D
D
F
F
D
D
F
F
D
D
D
Scraper Ring 1
9.8m
PU 161
PU 204

Fig. 4

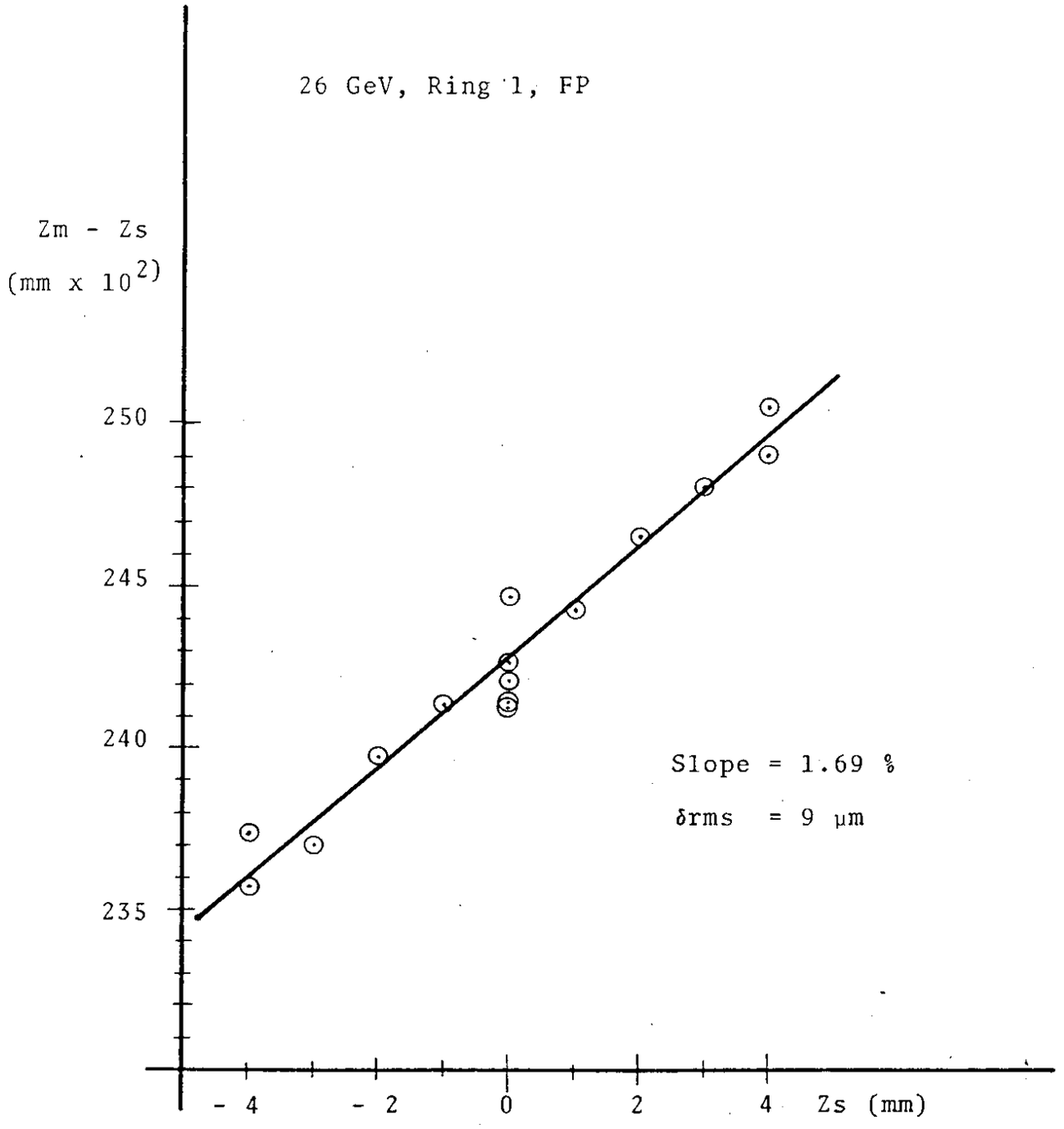
26 GeV, Ring 1, FP
Zm - Zs
(mm x 10 2)
250
245
240
235
Slope = 1.69 %
δrms = 9 μm
- 4
- 2
0
2
4
Zs (mm)

Fig. 5

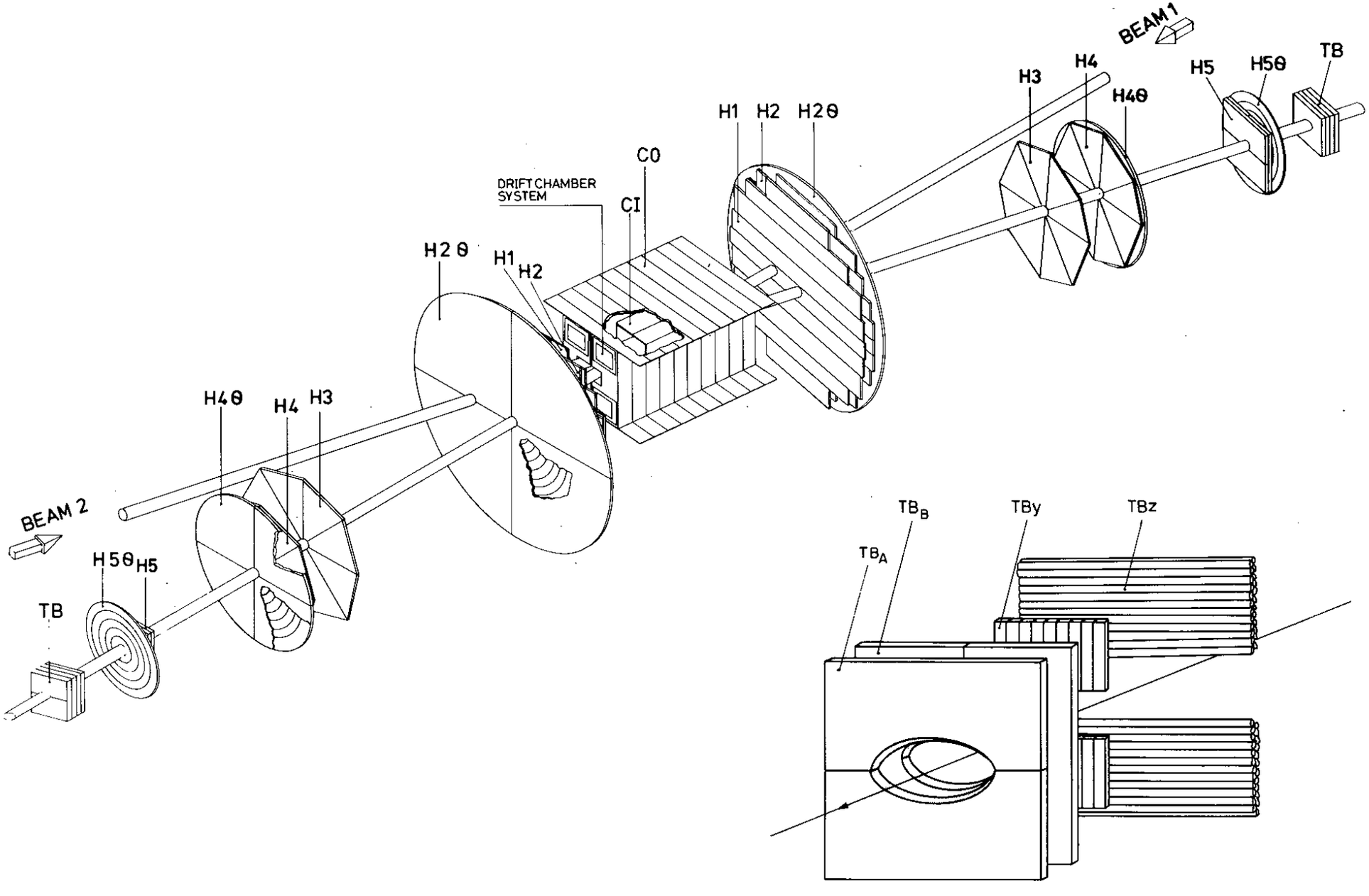
BEAM 1
BEAM 2
H1
H2
H2θ
H3
H4
H4θ
H5
H5θ
TB
C0
CI
DRIFT CHAMBER SYSTEM
TB_A
TB_B
TBy
TBz

Fig. 6

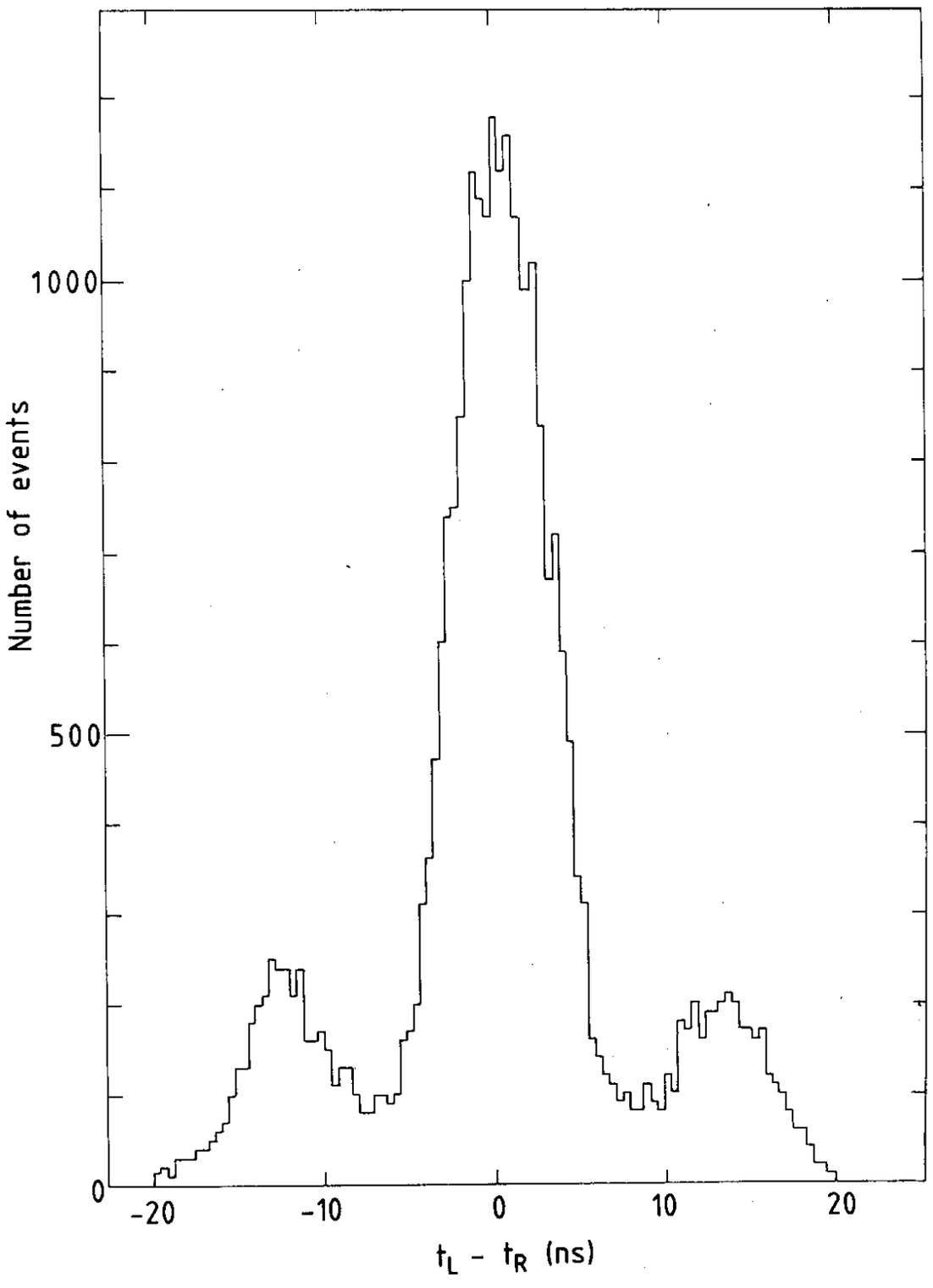

Fig. 7

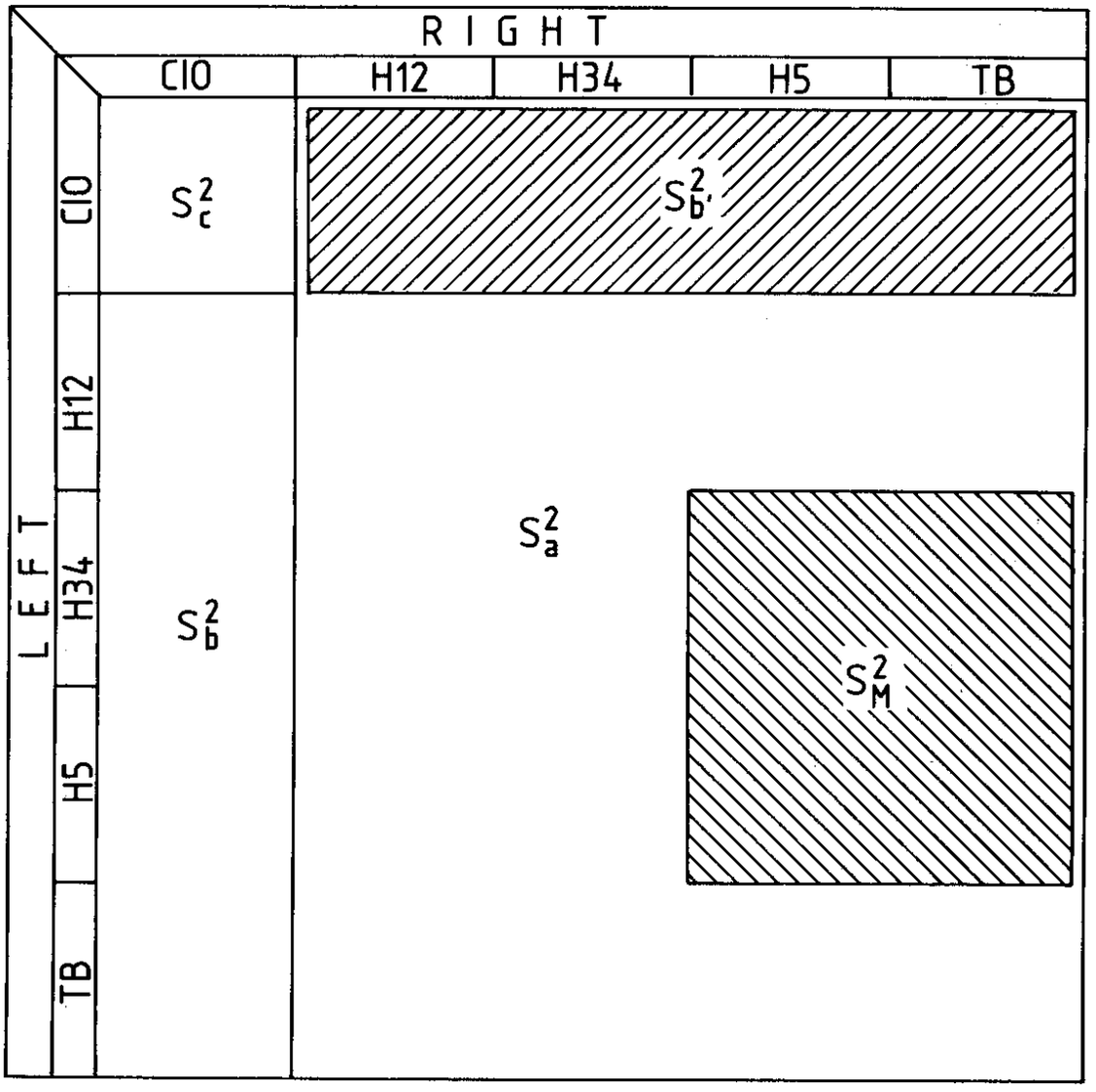
RIGHT
C10
H12
H34
H5
TB
LEFT
C10
H12
H34
H5
TB
S_c^2
$S_{b'}^2$
S_b^2
S_a^2
S_M^2

Fig. 8

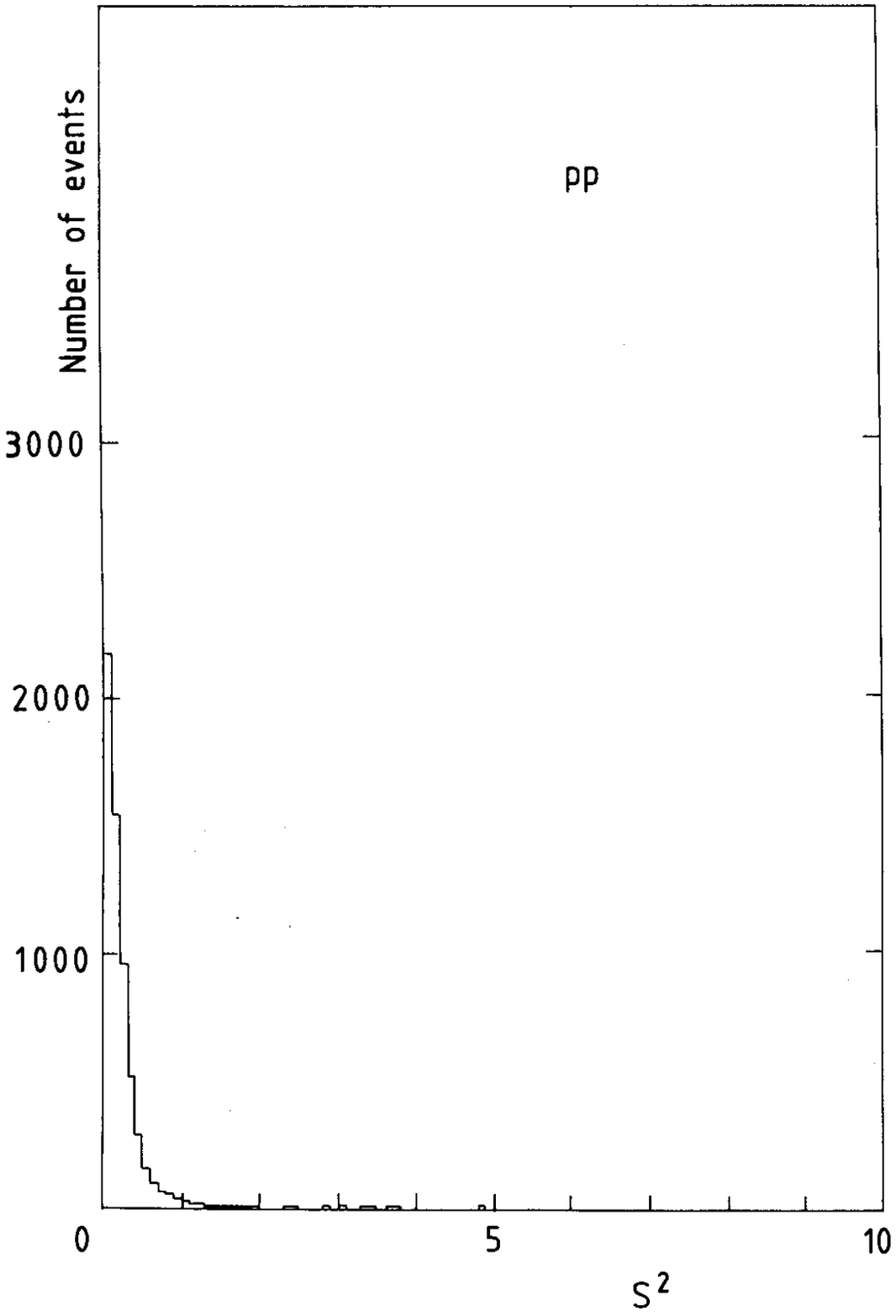

Fig. 9a

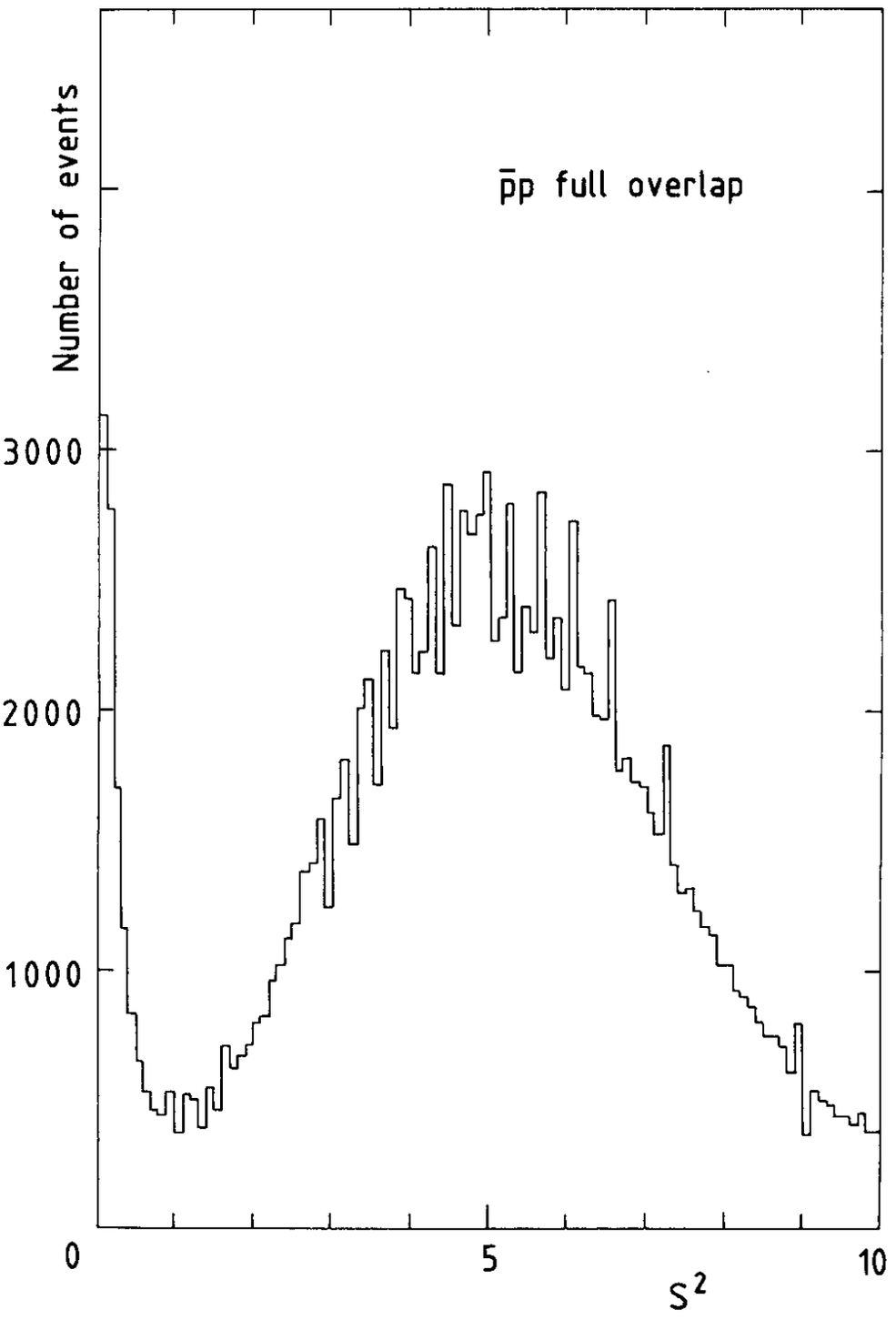

Fig. 9b

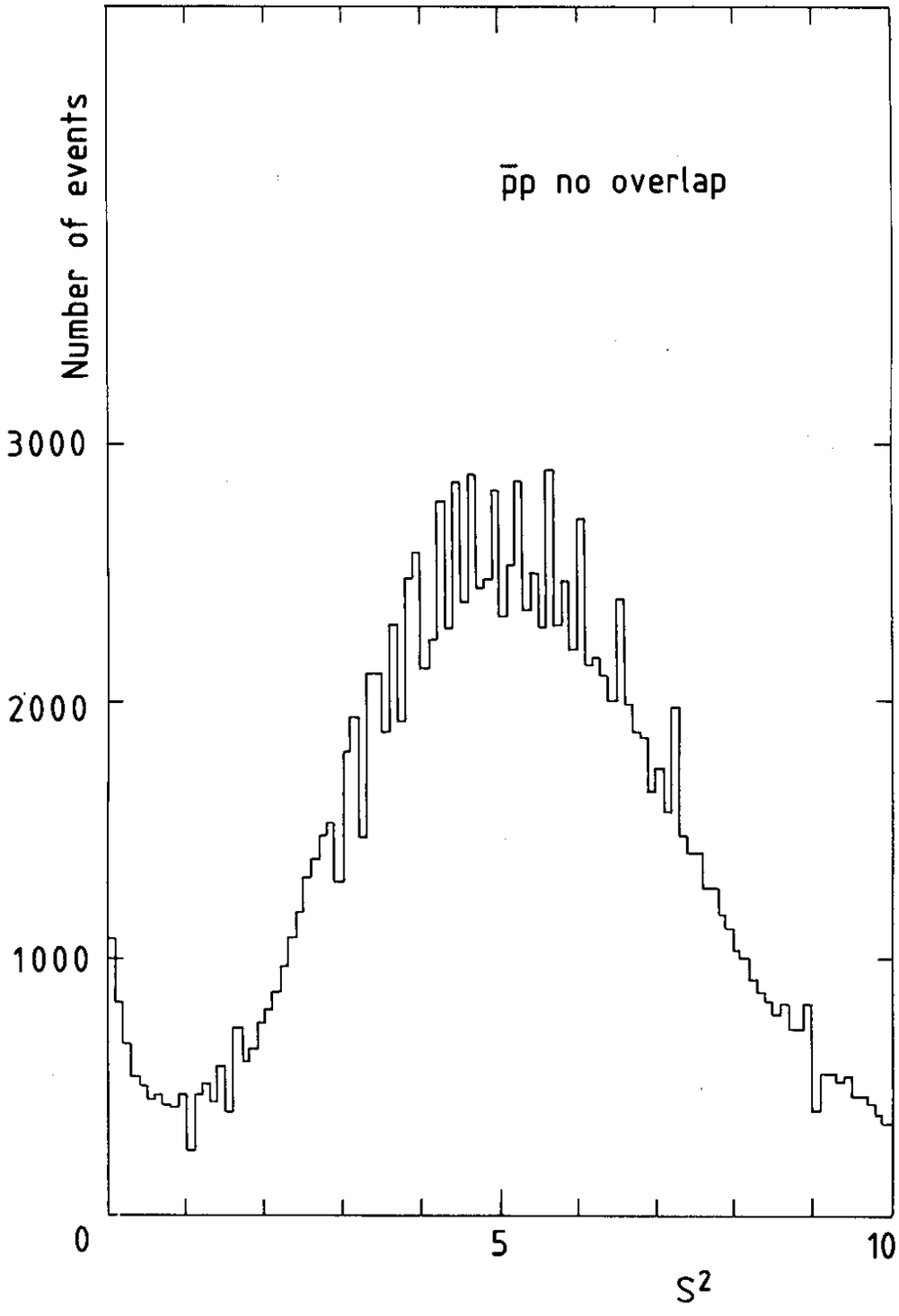

Fig. 9c

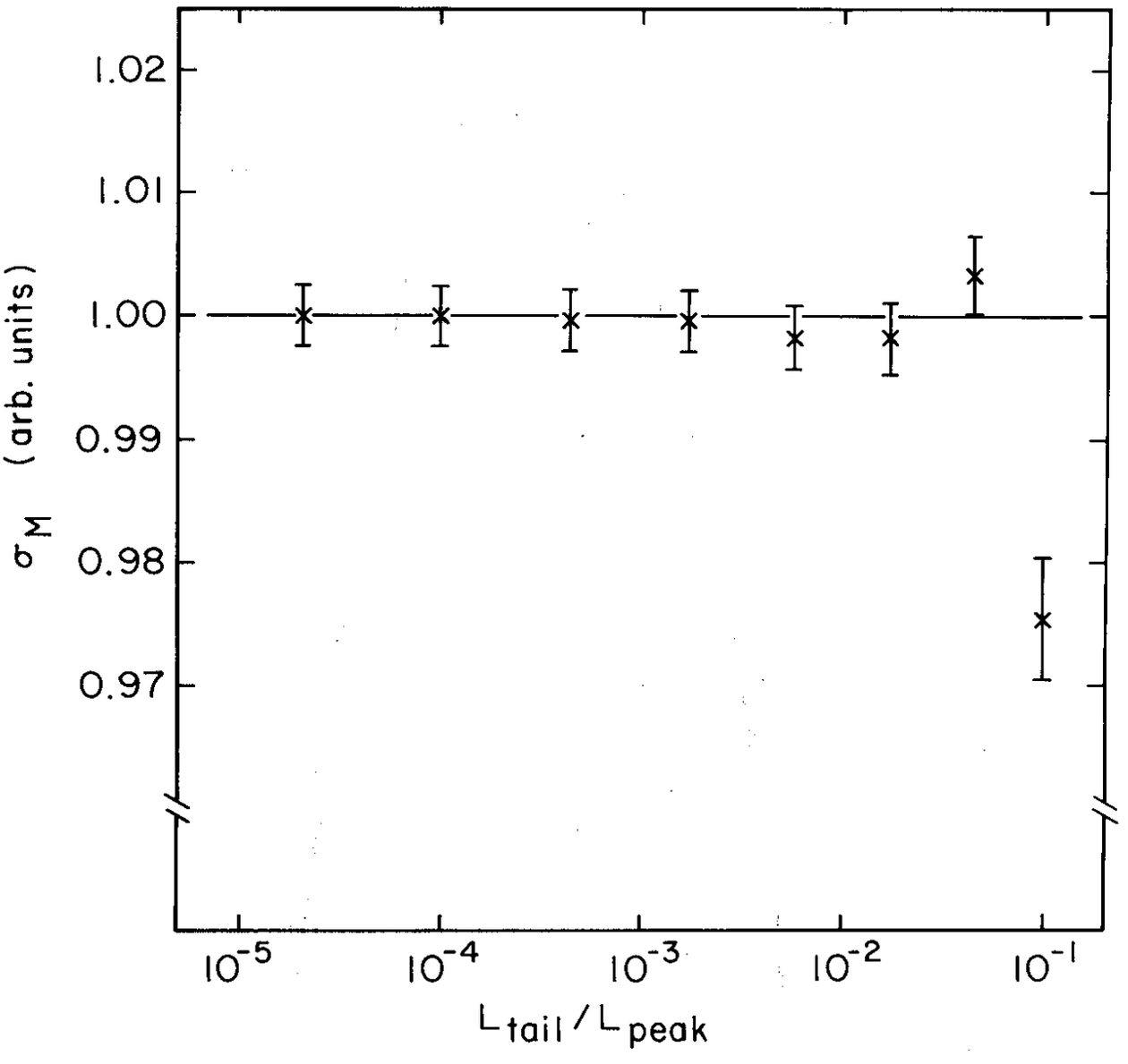
1.02
1.01
1.00
0.99
0.98
0.97
σM (arb. units)
10-5
10-4
10-3
10-2
10-1
Ltail / Lpeak

Fig. 10

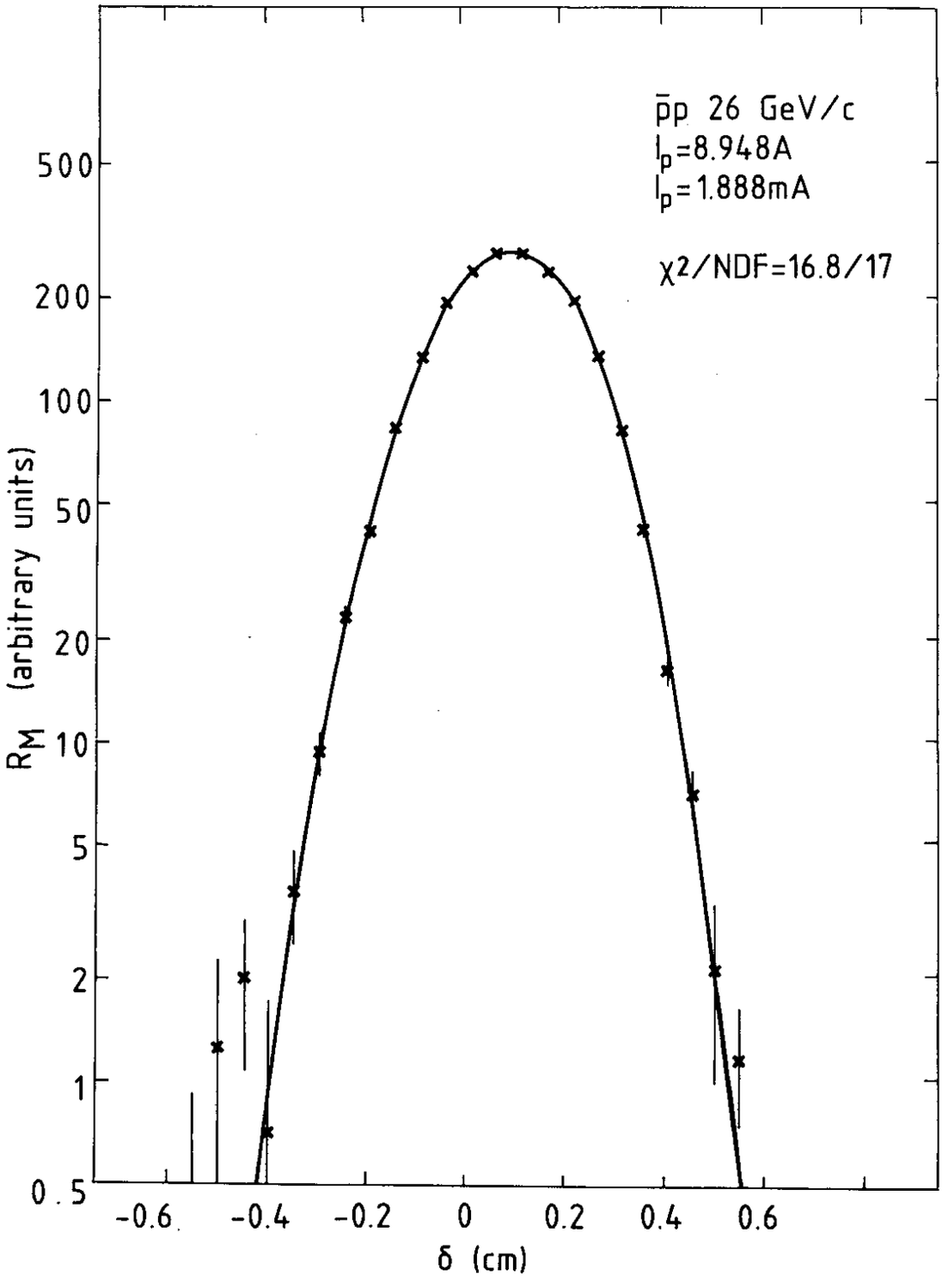
$\bar{p}p$ 26 GeV/c
I_p=8.948A
I_p=1.888mA
χ^2/NDF=16.8/17
500
200
100
50
20
10
5
2
1
0.5
R_M (arbitrary units)
-0.6
-0.4
-0.2
0
0.2
0.4
0.6
δ (cm)

Fig. 11

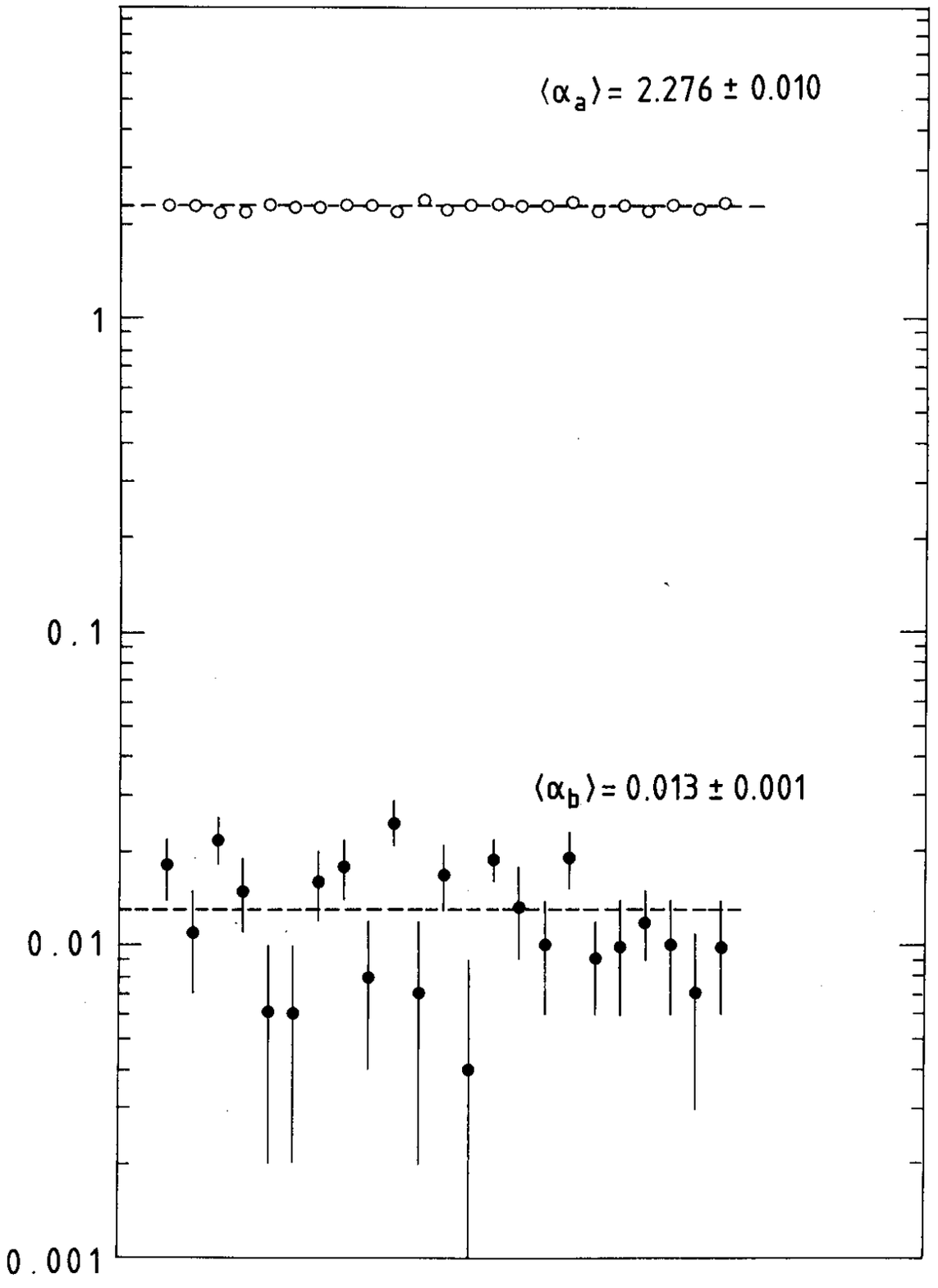

Fig. 12

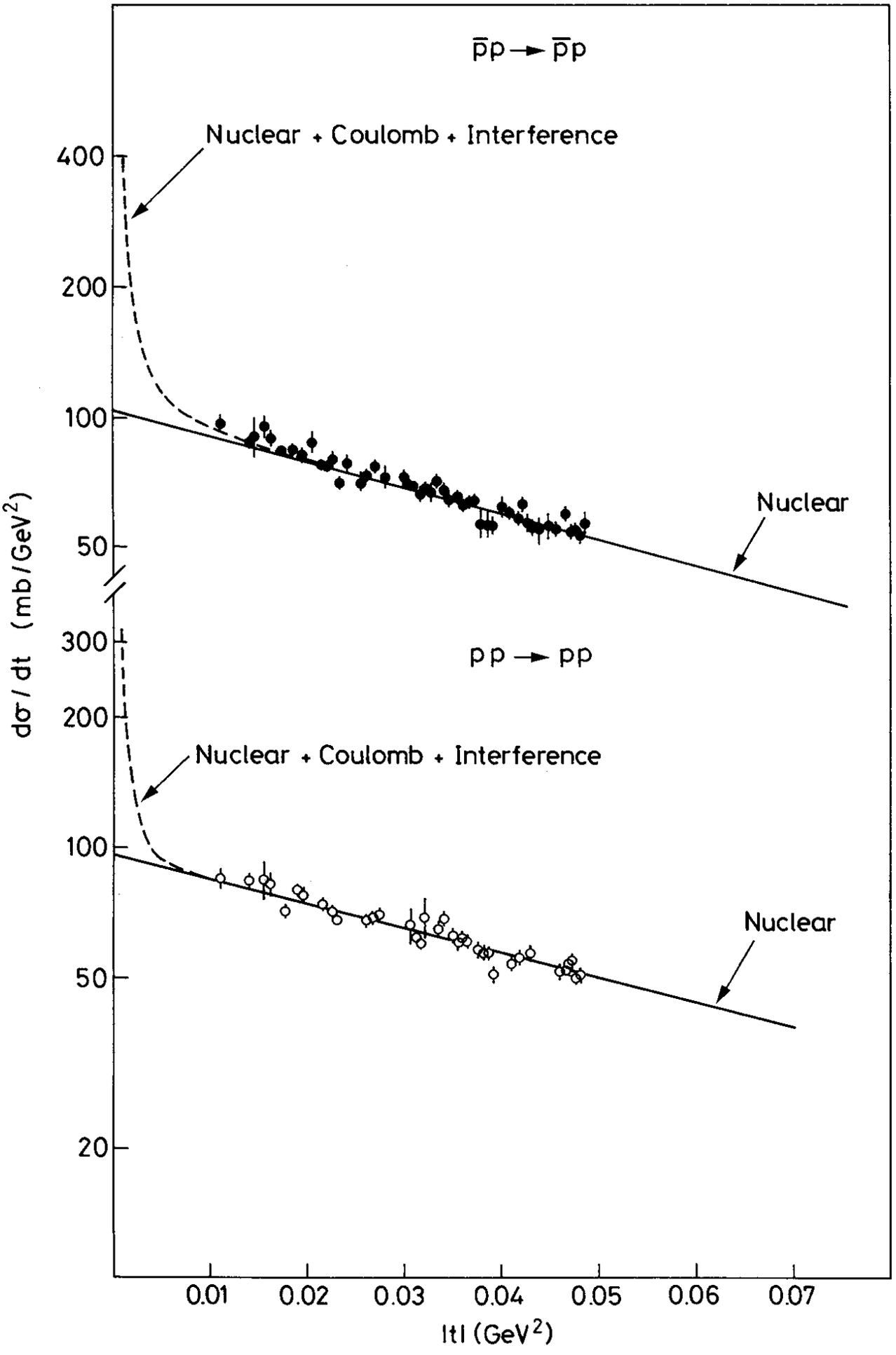
$\bar{p}p \rightarrow \bar{p}p$
Nuclear + Coulomb + Interference
Nuclear
$pp \rightarrow pp$
Nuclear + Coulomb + Interference
Nuclear
400
200
100
50
300
200
100
50
20
$d\sigma/dt$ (mb/GeV^2)
0.01
0.02
0.03
0.04
0.05
0.06
0.07
$|t|$ (GeV^2)

Fig. 13

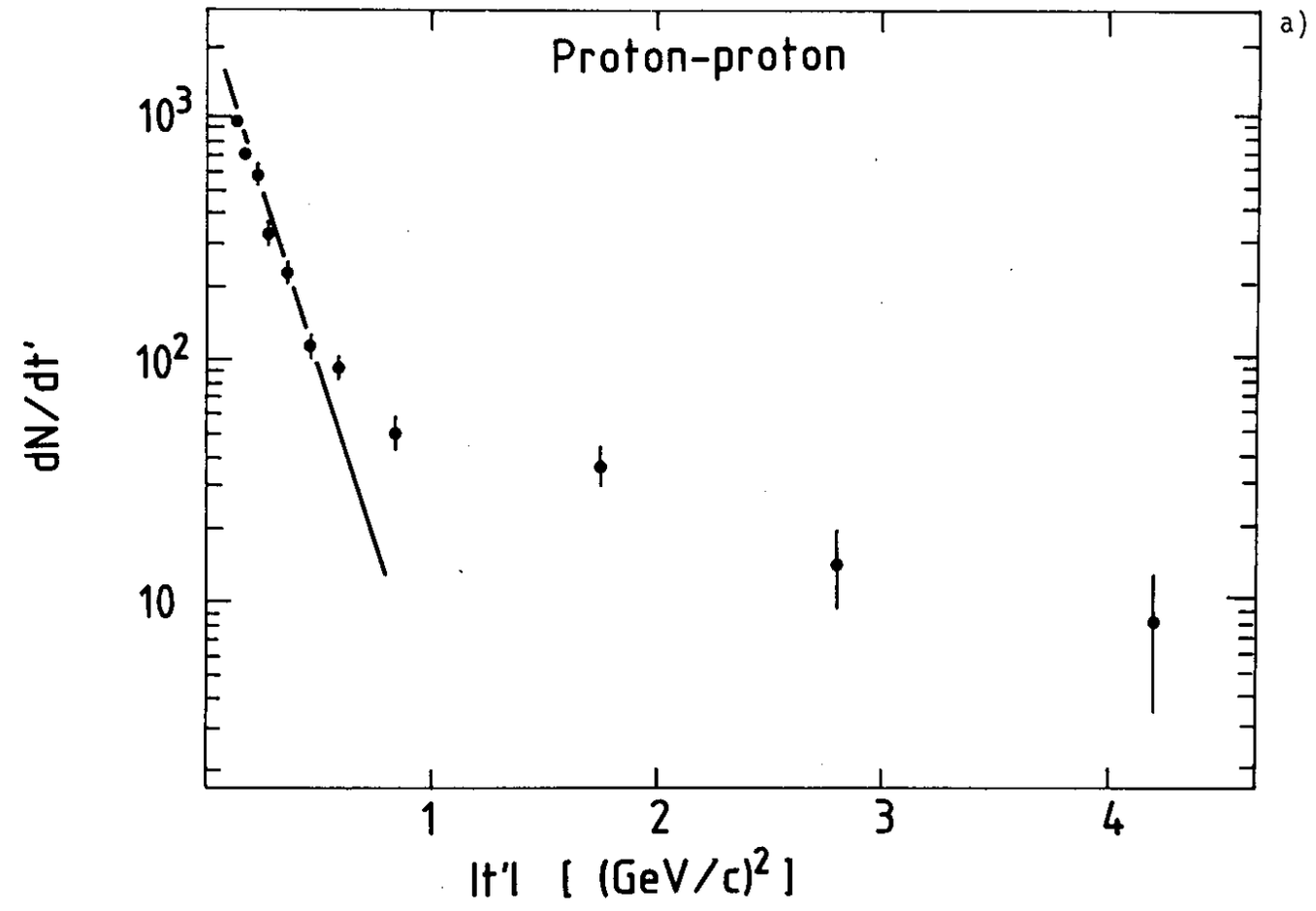
a)
Proton-proton
10^3
10^2
10
dN/dt'
1
2
3
4
|t'| [(GeV/c)^2]

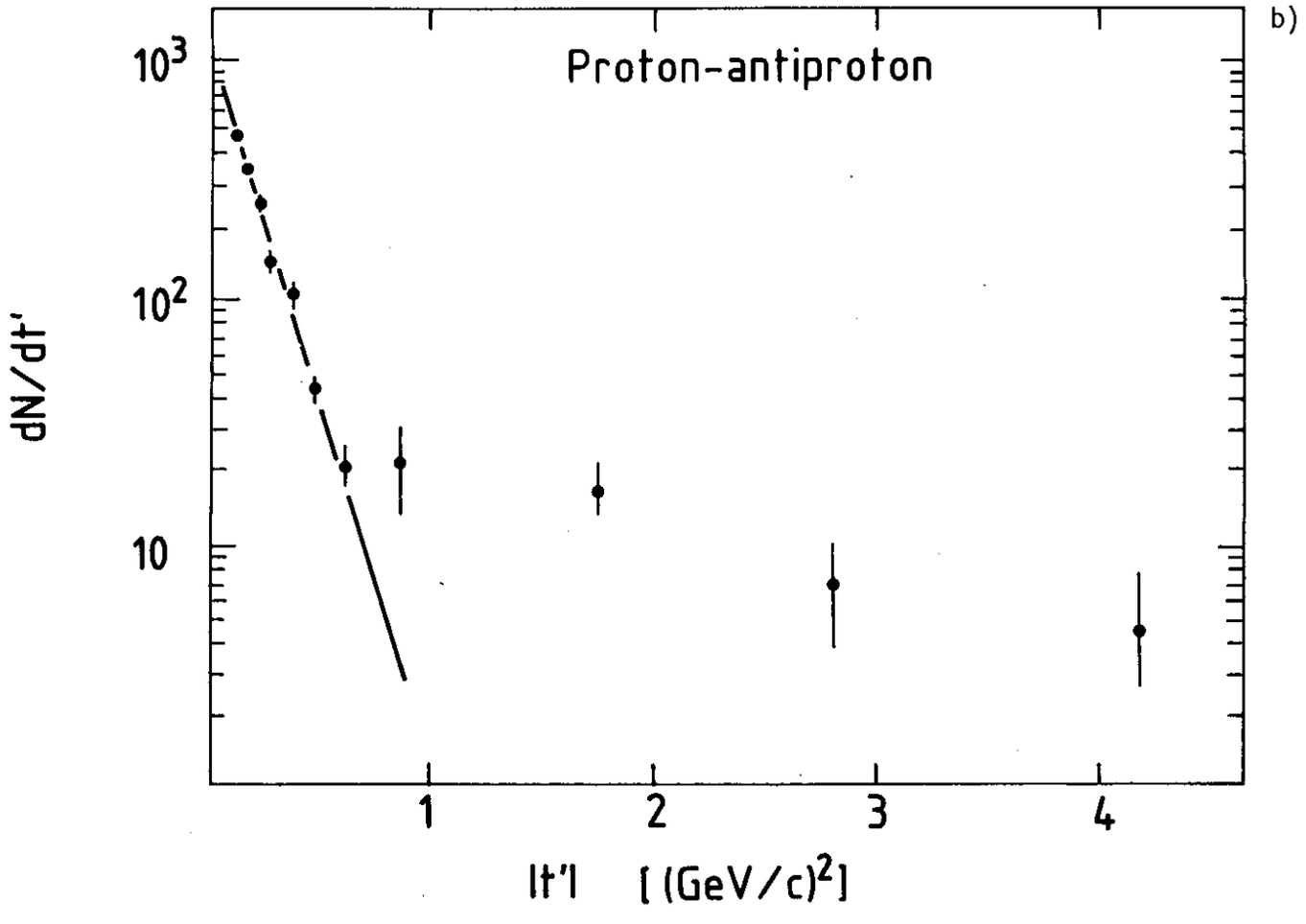
b)
Proton-antiproton
10^3
10^2
10
dN/dt'
1
2
3
4
|t'| [(GeV/c)^2]

Fig. 14

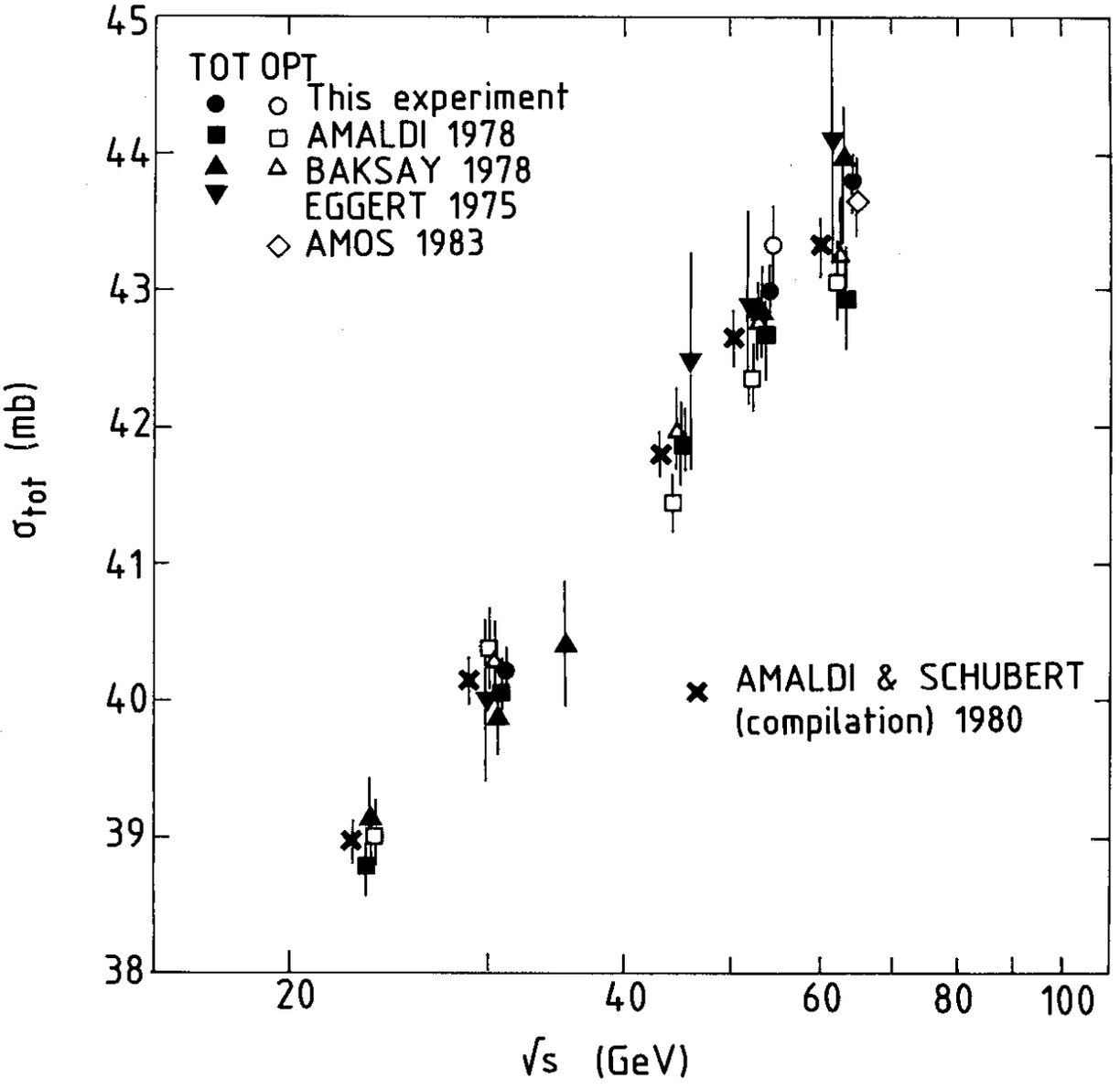
TOT OPT
This experiment
AMALDI 1978
BAKSAY 1978
EGGERT 1975
AMOS 1983
AMALDI & SCHUBERT
(compilation) 1980
σ_{tot} (mb)
$\sqrt{s}$ (GeV)
45
44
43
42
41
40
39
38
20
40
60
80
100

Fig. 15

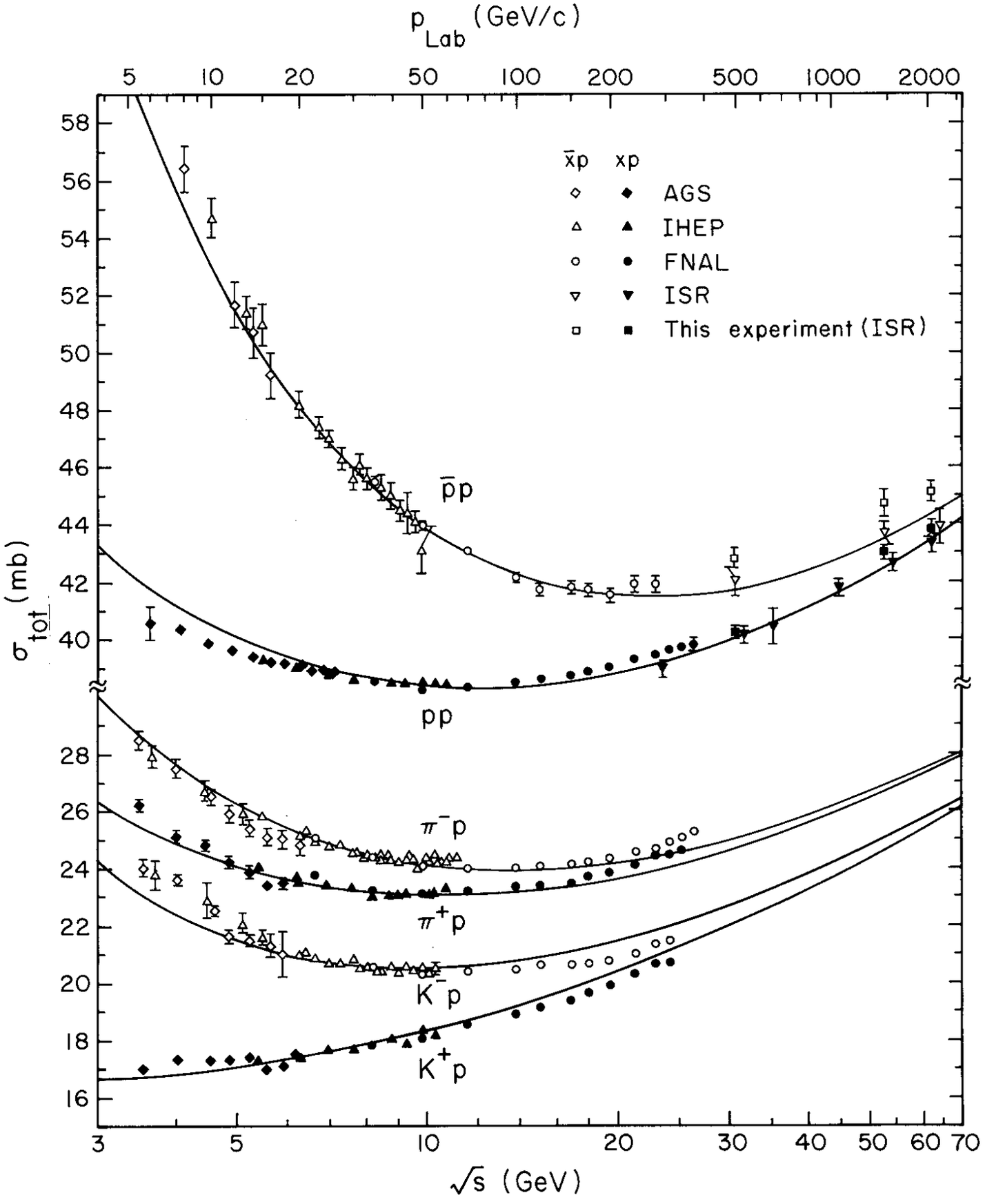
p Lab (GeV/c)
5
10
20
50
100
200
500
1000
2000
σ tot (mb)
58
56
54
52
50
48
46
44
42
40
28
26
24
22
20
18
16
x̄p xp
AGS
IHEP
FNAL
ISR
This experiment (ISR)
p̄p
pp
π⁻p
π⁺p
K⁻p
K⁺p
3
5
10
20
30
40
50
60
70
√s (GeV)

Fig. 16

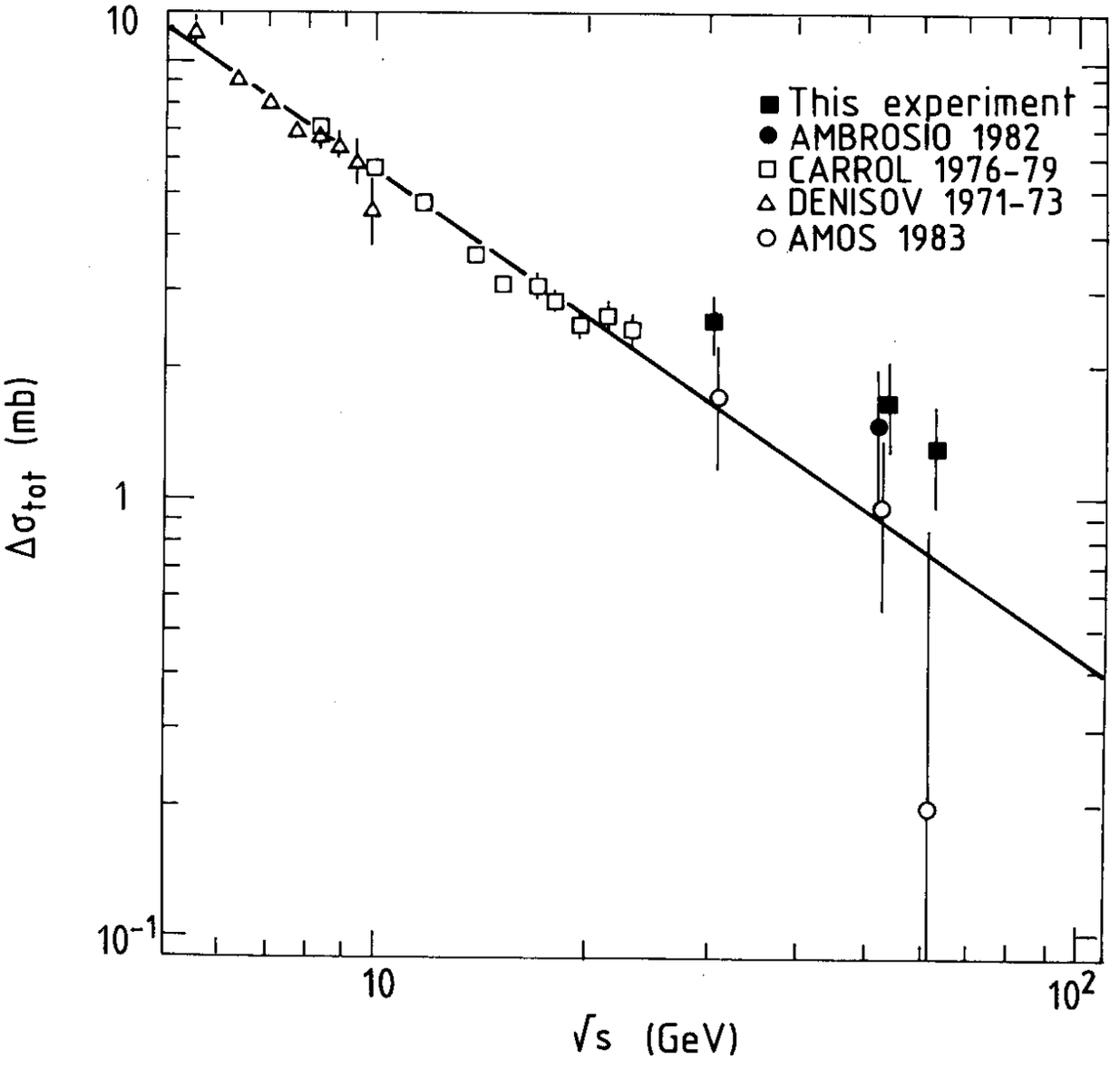
10
1
10^{-1}
$\Delta\sigma_{tot}$ (mb)
10
10^2
$\sqrt{s}$ (GeV)
This experiment
AMBROSIO 1982
CARROL 1976-79
DENISOV 1971-73
AMOS 1983

Fig. 17

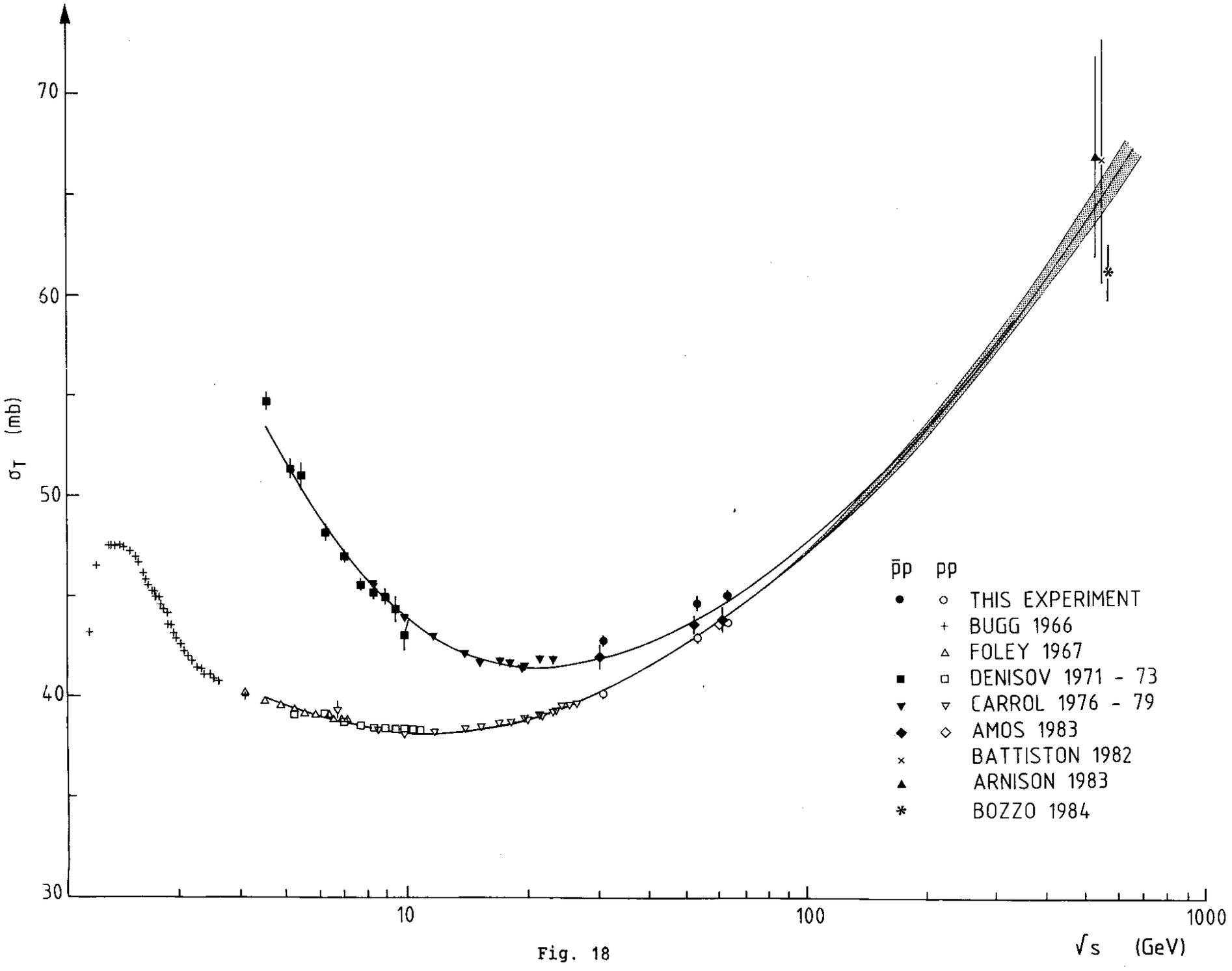
70
60
50
40
30
σ_T (mb)
10
100
1000
$\sqrt{s}$ (GeV)
$\bar{p}p$ pp
THIS EXPERIMENT
BUGG 1966
FOLEY 1967
DENISOV 1971 - 73
CARROL 1976 - 79
AMOS 1983
BATTISTON 1982
ARNISON 1983
BOZZO 1984

Fig. 18